Cell Reports

Resource

Lipid molecular timeline profiling reveals diurnal crosstalk between the liver and circulation

Graphical Abstract

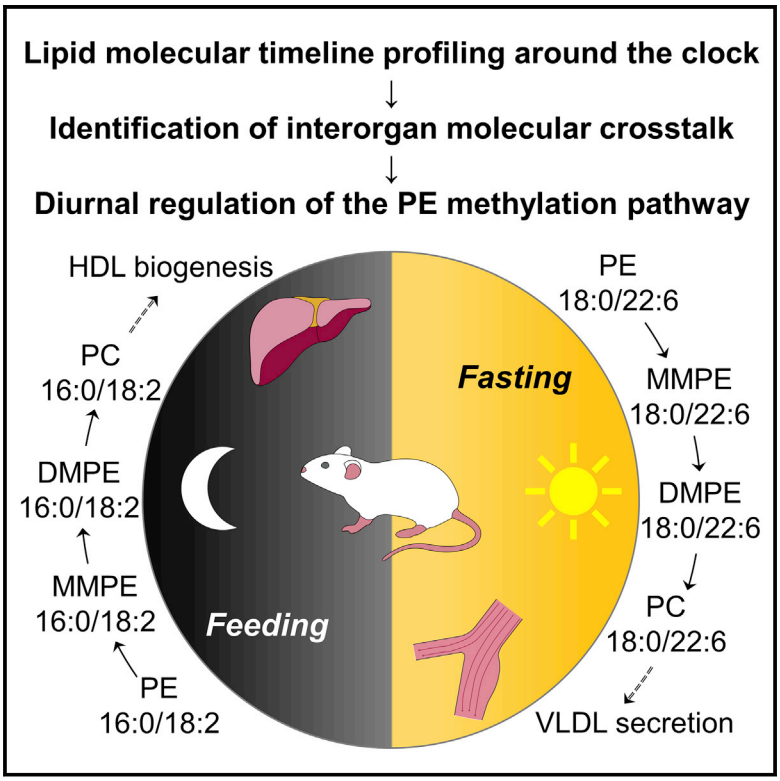

Highlights

- A framework for investigating fasting-feeding cycles and circadian rhythms
- Time-series analysis shows molecular oscillations are set by fasting-feeding cycles
- In-depth lipidomics provides insights into metabolic crosstalk between tissues
- Diurnal regulation of the hepatic PE methylation pathway and lipoprotein secretion

Authors

Richard R. Sprenger, Martin Hermansson, Ditte Neess, ..., Nils J. Færgeman, Robin W. Klemm, Christer S. Ejsing

Correspondence

cse@bmb.sdu.dk

In Brief

Sprenger et al. generate a time-resolved multi-omics resource of liver and plasma and find that molecular oscillations are entrained by fasting-feeding cycles. The authors go on to uncover that the hepatic PE methylation pathway is diurnally regulated and gives rise to two pools of oscillating PC molecules in the circulation.

Sprenger et al., 2021, Cell Reports *34*, 108710
February 2, 2021 © 2021 The Author(s).
https://doi.org/10.1016/j.celrep.2021.108710

CellPress

Cell Reports

CellPress
OPEN ACCESS

Resource

Lipid molecular timeline profiling reveals diurnal crosstalk between the liver and circulation

Richard R. Sprenger,[1,8] Martin Hermansson,[1,8] Ditte Neess,[1,8] Lena Sokol Becciolini,[1,8] Signe Bek Sørensen,[1] Rolf Fagerberg,[2] Josef Ecker,[3] Gerhard Liebisch,[4] Ole N. Jensen,[1] Dennis E. Vance,[5] Nils J. Færgeman,[1] Robin W. Klemm,[6] and Christer S. Ejsing[1,7,9,*]

[1]Department of Biochemistry and Molecular Biology, VILLUM Center for Bioanalytical Sciences, University of Southern Denmark, Odense, Denmark
[2]Department of Mathematics and Computer Science, University of Southern Denmark, Odense, Denmark
[3]ZIEL-Institute for Food & Health, Research Group Lipid Metabolism, Technical University of Munich, Freising, Germany
[4]Institute of Clinical Chemistry and Laboratory Medicine, Regensburg University Hospital, Regensburg, Germany
[5]Group on Molecular and Cell Biology of Lipids, University of Alberta, Edmonton, AB, Canada
[6]Department of Physiology, Anatomy and Genetics, University of Oxford, Oxford, UK
[7]Cell Biology and Biophysics Unit, European Molecular Biology Laboratory, Heidelberg, Germany
[8]These authors contributed equally
[9]Lead contact
*Correspondence: cse@bmb.sdu.dk
https://doi.org/10.1016/j.celrep.2021.108710

SUMMARY

Diurnal regulation of whole-body lipid metabolism plays a vital role in metabolic health. Although changes in lipid levels across the diurnal cycle have been investigated, the system-wide molecular responses to both short-acting fasting-feeding transitions and longer-timescale circadian rhythms have not been explored in parallel. Here, we perform time-series multi-omics analyses of liver and plasma revealing that the majority of molecular oscillations are entrained by adaptations to fasting, food intake, and the postprandial state. By developing algorithms for lipid structure enrichment analysis and lipid molecular crosstalk between tissues, we find that the hepatic phosphatidylethanolamine (PE) methylation pathway is diurnally regulated, giving rise to two pools of oscillating phosphatidylcholine (PC) molecules in the circulation, which are coupled to secretion of either very low-density lipoprotein (VLDL) or high-density lipoprotein (HDL) particles. Our work demonstrates that lipid molecular timeline profiling across tissues is key to disentangling complex metabolic processes and provides a critical resource for the study of whole-body lipid metabolism.

INTRODUCTION

Regulation and coordination of lipid metabolism at the whole-body level and around the diurnal cycle is of paramount importance for metabolic health. This regulation serves to modulate tissue-specific processes in response to changing physiological states that, during the day, alternate between periods of ample food intake and intermittent fasting. Dysregulation of diurnal cycles is linked to metabolic diseases, such as obesity, hyperlipidemia, fatty liver, and type 2 diabetes (Panda, 2019; Saran et al., 2020). Despite the enormous medical relevance and societal impact of these conditions, the spatiotemporal regulation of lipid metabolism is not well understood at the molecular level. Quantitative lipid metabolic profiling within tissues and characterization of molecular crosstalk between organs are central to better understanding of the mechanisms controlling whole-body homeostasis.

More than a century of research has uncovered the general concepts underlying regulation of whole-body lipid metabolism across fasting-feeding cycles. A prominent metabolic hallmark of fasting is the cycling of non-esterified fatty acids (NEFAs) and triacylglycerols (TAGs) between adipose tissue and the liver (Reshef et al., 2003). This process results from increased lipolysis of TAGs in adipose tissue and release of NEFAs into the circulation. In the liver, NEFAs can be used for energy production and synthesis of TAGs, which become incorporated into very low-density lipoprotein (VLDL) particles and secreted for transport back to adipose tissue. Here, TAGs are again hydrolyzed, and NEFAs are taken up and esterified into TAGs. The importance of the TAG-NEFA cycle is exemplified by the treatment of type 2 diabetes with thiazolidinediones, which attenuates this process by increasing the TAG storage capacity of adipocytes, thereby reducing the NEFA release and ameliorating hyperlipidemia and insulin resistance (Soccio et al., 2014). During feeding and the subsequent postprandial state, prominent metabolic hallmarks, mediated by fast-acting insulin signaling, are attenuation of lipolysis in adipose tissue (Frayn, 2002) and increased *de novo* lipogenesis in hepatocytes and adipocytes (Wallace and Metallo, 2020). Moreover, dietary fats are incorporated into chylomicrons, which are transported from the intestine via the lymph and circulation to adipose tissue for storage as TAGs (Bickerton et al., 2007). Overall, these metabolic states

This is an open access article under the CC BY license (http://creativecommons.org/licenses/by/4.0/).

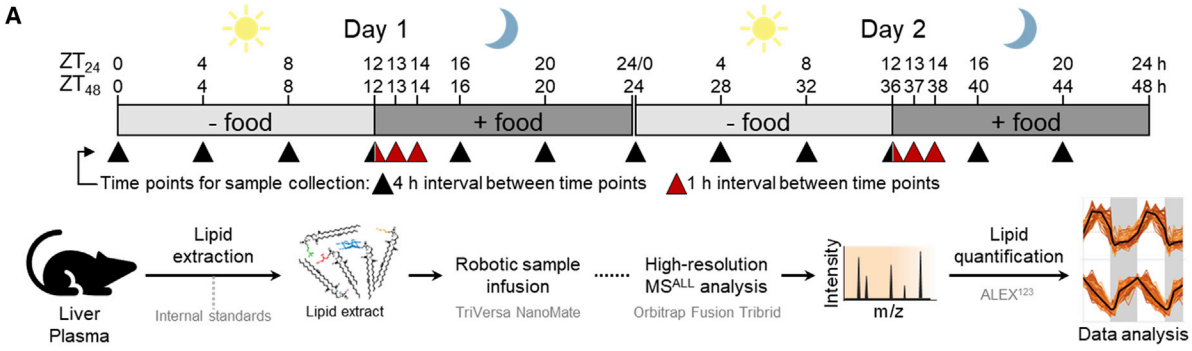

B

Liver lipidome coverage	Adamovich et al. 2014	Current study
# lipid categories	4	5
# lipid classes	12	33
# lipid molecules	159	1177

Statistics	JTK_CYCLE $p < 0.05$	Interday Pearson $r > 0.66$ and ANOVA $p < 0.05$
# oscillating lipid molecules	27 (17%)	587 (50%)

Data metrics	Adamovich et al. 2014	Current study
# diurnal cycles (24 h)	1	2
# time points/diurnal cycle	6	8
Time intervals	4 h	1-2-4 h
# replicates/time point/cycle	4	6

C

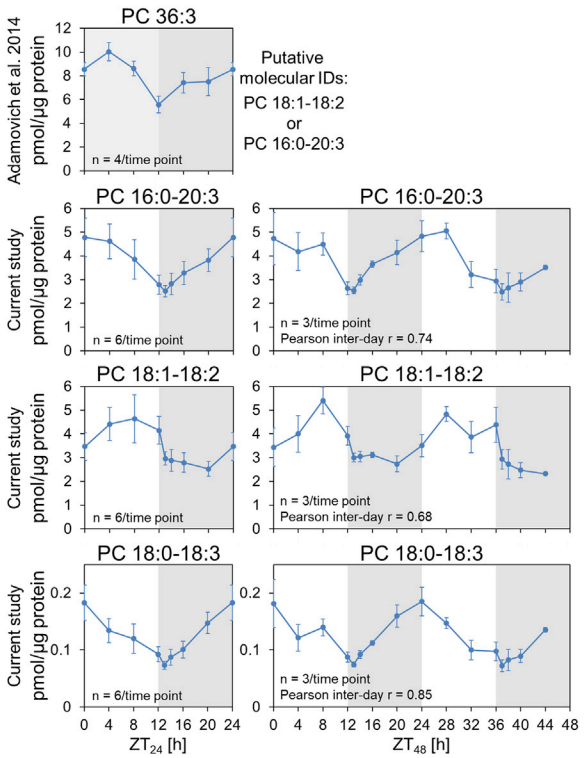

D

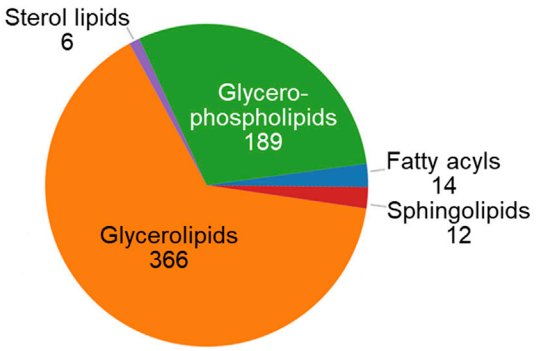

E

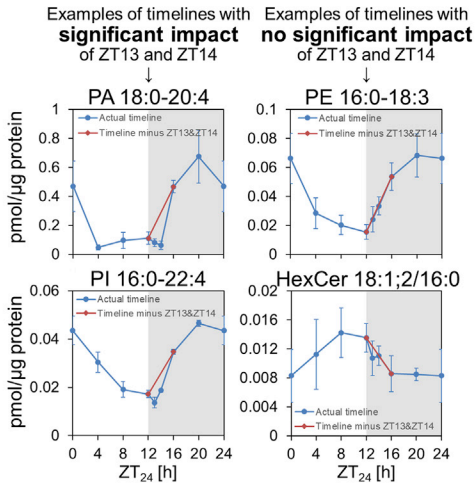

F

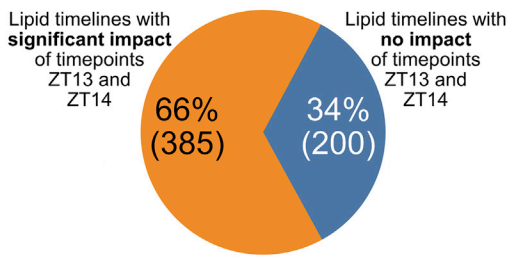

(legend on next page)

highlight the importance of diurnal regulation of lipid transport between metabolically linked organs, and specifically, that this crosstalk is coupled to dynamic changes in lipid molecular signatures in the circulation. Precise time-resolved analysis of the blood plasma lipidome and exact knowledge of individual lipid metabolic trajectories between tissues can therefore serve as a diagnostic window into the metabolic fitness of an entire system of organs.

More recently, diurnal regulation of lipid metabolism has also been ascribed to longer-timescale cell-autonomous circadian clocks that produce a 24-h self-sustained rhythmic transcription of target genes (Reddy and O'Neill, 2010). Some evidence exists that this mode of regulation results in ~15% of lipids undergoing sinusoid-like changes in mouse and human plasma, liver, and skeletal muscle (Adamovich et al., 2014; Chua et al., 2013; Dallmann et al., 2012; Eckel-Mahan et al., 2013; Held et al., 2020; Isherwood et al., 2017; Loizides-Mangold et al., 2017; Minami et al., 2009). These studies have, however, been focused on capturing oscillations over longer time frames, using regular 3- to 4-h interval sampling, and responses over shorter timescales related to short-acting fasting-feeding transitions might have inadvertently been missed. Furthermore, due to technical limitations, these studies report moderate lipidome coverage where lipids are identified at the so-called species-level (e.g., PC 34:2), instead of reporting at the molecular species-level by identifying the composition of individual fatty acyl (FA) chains (e.g., PC 16:0–18:2, PC 16:1–18:1) (Liebisch et al., 2013). Adding this deeper layer of lipid structural information provides a considerable mechanistic depth to our understanding of metabolic trajectories of individual lipid molecules and their crosstalk between tissues.

Here, we examined diurnal oscillations in the mouse liver and plasma lipidomes, as well as the liver proteome, using a framework that in parallel captures responses to short-acting fasting-feeding transitions and longer-timescale circadian rhythms. Our data reveal that 50%, 79%, and 20% of the liver lipidome, plasma lipidome, and liver proteome, respectively, display diurnal oscillations, and that 66% of the liver lipidome oscillations are governed by adaptation to food intake. Beyond these unexpected global patterns, we also uncover a distinct mode of diurnal crosstalk where hepatic production of PC by methylation of PE gives rise to two pools of oscillating PC molecules in the circulation: 22:6-containing PCs that are produced by the methyltransferase Pemt and are coupled to VLDL secretion, and 18:2-containing PCs that are likely produced by an unknown methyltransferase and are coupled to production of HDL particles. Altogether, this study demonstrates the power of molecular lipid timeline profiling to identify mechanisms underlying complex lipid metabolic processes and provides a valuable resource for the study of diurnal regulation of whole-body lipid metabolism and homeostasis.

RESULTS

Framework for capturing responses to fasting-feeding transitions and circadian rhythms

To explore how lipid metabolic crosstalk between the liver and circulation is controlled by short-acting fasting-feeding transitions and longer-timescale circadian rhythms, we devised a framework that accommodates both regular 4-h interval sampling over two diurnal cycles (i.e., 48 h) and more frequent sampling with 1-h intervals at the onset of feeding (Figure 1A). Specifically, we collected samples of liver and plasma every 4 h from three individual mice during the day when mice are fasting (i.e., at zeitgeber time [ZT_{24}] = 0, 4, 8, 12 h). Moreover, during the nocturnal period when mice are feeding, we collected samples over intervals of 1, 2, and 4 h (i.e., at ZT_{24} = 13, 14, 16, 20 h). This design uniquely enables time-series analysis with 16 time points and three biological replicates across two diurnal cycles (i.e., 48 h), which is required to ascertain true diurnal oscillations (Hughes et al., 2017), as well as stringent statistical analysis over eight time points with six biological replicates covering a single diurnal period (i.e., 24 h). We note that nighttime-restricted feeding modulates whole-body energy metabolism differently as compared with *ad libitum* fed mice (Bray et al., 2013), and that this improves metabolic health and physiological rhythms (Chaix et al., 2019; Hatori et al., 2012). Moreover, mice on this dietary regimen consume a bigger meal during the first 1–2 h at onset of nighttime when food is provided (i.e., ZT_{24} = 12 h) and then occasionally consume smaller portions for the remainder of the nocturnal period until the food is withdrawn at onset of daytime (Bray et al., 2013).

Extensive remodeling of the liver lipidome

To obtain a temporal depiction of the liver lipidome, we performed in-depth MS^{ALL} lipidomics of the collected liver samples. MS^{ALL} analysis is a lipidomics technology that affords high-fidelity identification and accurate quantification of molecular lipid species using high-resolution tandem mass spectrometry (Figures 1A and S1A) (Almeida et al., 2015; Freyre et al., 2019; Gallego et al., 2018). Overall, we quantified (i.e., pmol/μg protein)

Figure 1. Diurnal oscillations in the mouse liver lipidome

(A) Schematic of the experimental framework and lipidomics workflow. Mice were subjected to nighttime-restricted feeding (indicated in gray). Liver and plasma samples were collected at the indicated zeitgeber time (ZT) points (indicated by triangles) across two diurnal cycles. At the onset of feeding, samples were collected every hour (indicated by red triangles). Three mice were euthanized per time point. Liver and plasma samples were analyzed by in-depth MS^{ALL} lipidomics.

(B) Lipidome coverage and relevant data metrics compared with data of Adamovich et al. (2014).

(C) MS^{ALL} analysis shows that oscillating PC 36:3 represents three molecular lipid species, each having a unique timeline. Data represent mean ± SD (based on indicated number of biological replicates per time point).

(D) Number of oscillating lipids distributed according to their lipid categories.

(E) Examples of oscillating lipids that are entrained by short-acting fasting-feeding cycles and longer-timescale circadian rhythms. Data represent mean ± SD (n = 6 biological replicates).

(F) Proportion of oscillating lipids that are entrained by fasting-feeding cycles and circadian rhythms. The grouping of lipids is based on one-sample t tests. See also Figure S1.

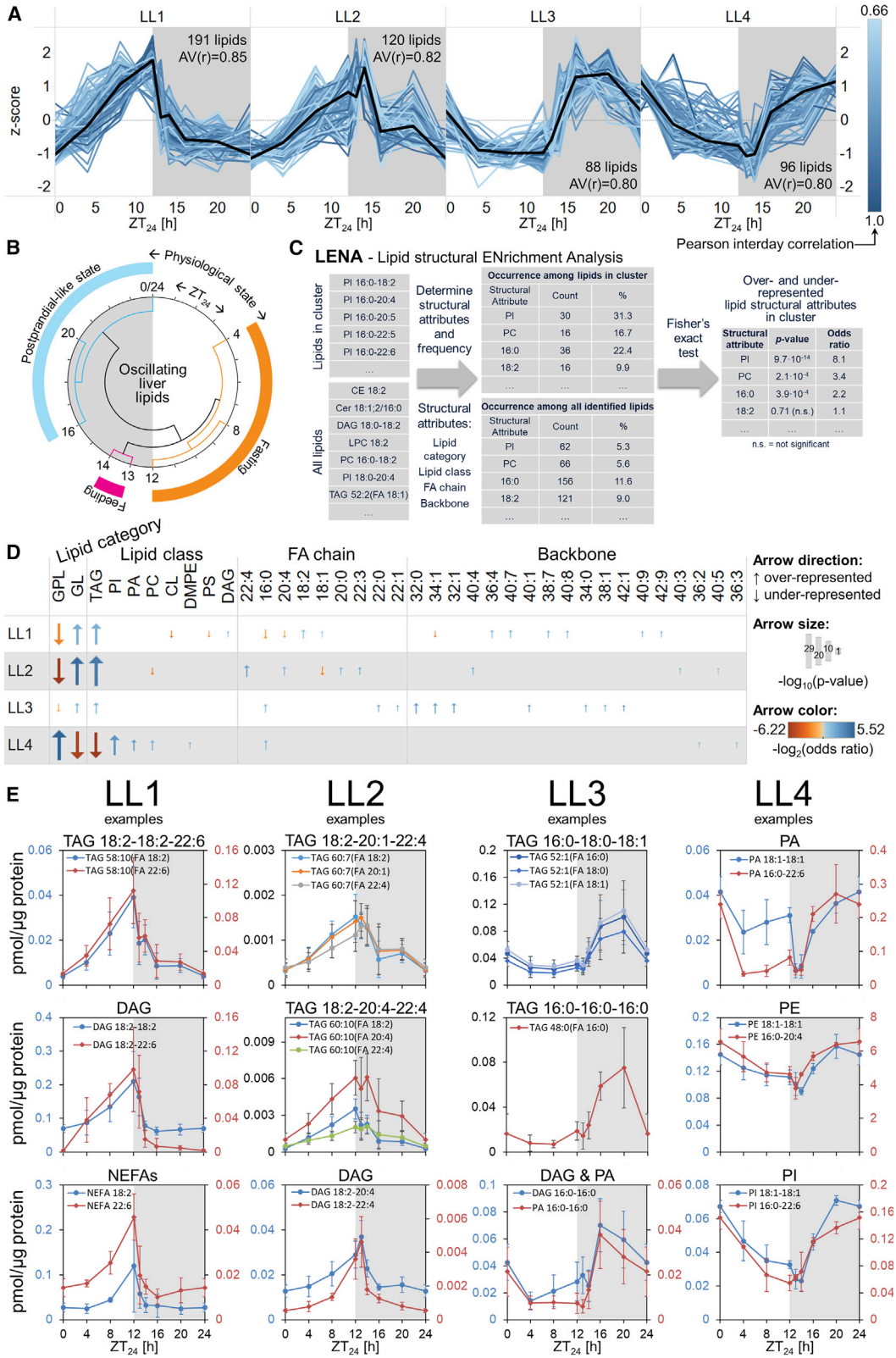

(legend on next page)

1,177 lipid molecules, encompassing 33 lipid classes (Figure 1B; Table S1). 1,006 (85%) lipid molecules were identified at the molecular species-level with individual hydrocarbon chains, and 171 (15%) lipids were identified at the species-level, with assignment of the total number of C atoms, double bonds, and hydroxyl groups in all hydrocarbon chains. This coverage exceeds that of a recent circadian lipidomics study both in extent and molecular detail (Adamovich et al., 2014) (Figure 1B). Specifically, our more extensive coverage stems from monitoring more lipid classes, as well as resolving numerous isomeric lipid molecules that were previously not distinguished.

For example, the lipid PC 36:3, exhibiting the most significant oscillations in previous data, was represented by a single timeline and ambiguously identified as PC 18:1–18:2 or PC 16:0–20:3 (Figure 1C). In our dataset, PC 36:3 is represented by three distinct timelines unambiguously ascribed to the molecular lipid species PC 18:1–18:2, PC 18:0–18:3, and PC 16:0–20:3 (Figure 1C). Notably, the timelines of PC 18:0–18:3 and PC 16:0–20:3 resemble that of PC 36:3 reported previously and are characterized by a gradual decrease during fasting at daytime, as well as an immediate increase upon the onset of feeding at nighttime. Unexpectedly, we found that the temporal profile of PC 18:1–18:2 contrasts with the two other PCs, hidden when these distinct molecules are tracked at the species level. Importantly, these data exemplify the deeper, more resolved lipid structural information captured by our MS^{ALL} technology.

Next, we examined the extent to which the liver lipidome is remodeled across the diurnal cycle. Given that the commonly used JTK_CYCLE algorithm for identifying circadian rhythmicity cannot process data with unequal time intervals like ours, we devised an alternative statistical algorithm to identify diurnal oscillations. First, we confirmed that lipid oscillations are truly repetitive and not due to random noise. To do so, we implemented a stringent filter, which is based on the Pearson correlation coefficient (r) between lipid abundances measured across the first and the second day, and rigorous inclusion of only lipids with an interday correlation greater than 0.66. Second, we carried out analysis of variance (ANOVA), finding that 50% of the liver lipidome, comprising 587 lipids, displays significant diurnal oscillations (i.e., $p < 0.05$ and $r > 0.66$) (Figure 1B). This represents a 22-fold increase in the identification of oscillating lipids in comparison with Adamovich et al. (2014), which, in combination with our greater lipidome coverage, improves the molecular insight dramatically.

The 587 oscillating lipid molecules include glycerolipids (62%), glycerophospholipids (32%), and to lesser extents, sphingolipids, sterol lipids, and FAs (Figure 1D). Inspecting the underlying lipid classes, we found that oscillations are most frequent among TAG (57%), followed by phosphatidylinositol (PI) (5.8%), PC (5.5%), and PE (3.9%) (Figure S1B). Interestingly, we also observed oscillation of low-abundance monomethyl-phosphatidylethanolamine (MMPE) and dimethyl-phosphatidylethanolamine (DMPE) molecules, which are intermediates in PC synthesis via the PE methylation pathway (Figure S1C). However, the final products, PCs with identical FA chains, do not display similar fluctuations. Thus, the in-depth lipidome analysis also allowed us to discern critical signatures of fluctuating metabolic events underlying the homeostasis of steady-state lipid levels.

Finally, we examined the ability of our framework to disentangle responses related to fasting-feeding transitions and longer-timescale circadian rhythms. To do so, we determined the number of lipids for which exclusion of the time points $ZT_{24} = 13$ and 14 h would significantly bias their actual temporal dynamics (Figure 1E). Strikingly, this revealed that the timelines of at least 66% of all oscillating lipids are adversely impacted if sampling is not performed at these time points (Figure 1F). Importantly, this also demonstrates that the dynamics of most lipids are primarily coupled to fasting-feeding cycles. Conversely, the remaining 34% of oscillations have temporal profiles similar to the sinusoid-like changes associated with circadian rhythms (Figures 1E and 1F).

Taken together, our data represent a high-quality resource of the mouse liver lipidome with unprecedented coverage and provide unparalleled molecular insight into the interplay between the diurnal cycle and the regulation of lipid metabolic activities. Importantly, our data uncover that 66% of oscillations are primarily entrained by short-acting fasting-feeding transitions. Furthermore, it demonstrates that our framework captures the impact of metabolic regulators operating at substantially different timescales, covering circadian rhythms and physiological adaptations to fasting-feeding cycles.

Four clusters of oscillating liver lipids

To determine whether the oscillating lipids display commonalties in their temporal dynamics, we carried out fuzzy c-means clustering (Schwämmle and Jensen, 2018). This revealed that the oscillating liver lipids (LLs) cluster into four major timelines: LL1, LL2, LL3, and LL4 (Figure 2A). Specifically, LL1 lipids show a gradual increase during daytime when mice are fasting and rapidly decrease when mice start feeding at onset of nighttime. LL2 lipids increase during fasting, albeit with a shallower incline compared with LL1 lipids, then abruptly decrease 2 h after the onset of feeding. LL3 lipids are rapidly reduced at onset of fasting and rapidly increase upon feeding until they plateau in the middle of the night. Finally, LL4 lipids display a shallower decline than LL3 lipids during fasting, then temporarily decrease at the onset of feeding, before increasing 2 h after onset of feeding.

Figure 2. Four major clusters of oscillating liver lipids

(A) Fuzzy c-means clustering of oscillating liver lipids. Number of lipids and their average Pearson correlation coefficient are denoted in individual plots.

(B) Hierarchical clustering of the liver lipid timeline clusters.

(C) Schematic of the LENA algorithm used for lipid structure enrichment analysis.

(D) Over- and under-represented structural attributes in the timeline clusters.

(E) Representative lipid molecular timelines of cluster members. Data represent median ± 95% confidence interval for the median of five to six biological replicates.

See also Figure S2.

Hierarchical clustering of these timelines further revealed that the liver lipidome transits through three temporal periods, each with distinct physiological traits (Figure 2B). Specifically, one period corresponds to fasting and comprises the time points ZT_{24} = 4, 8, and 12 h. This is followed by a period that reflects the onset of feeding and comprises the time points ZT_{24} = 13 and 14 h and, finally, a period that signifies a postprandial-like state and covers the time points ZT_{24} = 16, 20, and 0/24 h. Overall, these data argue that the liver lipidome oscillations, and the activity of the underlying metabolic machinery, primarily reflect physiological adaptations to fasting-feeding cycles. In turn, this gives rise to four timelines that signify early and late stages of fasting (i.e., LL1 and LL2 lipids, respectively), acute effects of food intake (i.e., LL3 lipids), and a postprandial-like state (i.e., LL4 lipids).

Each lipid cluster has distinct structural hallmarks

Next, we explored the lipid molecular signatures of the timeline clusters. Similar to Gene Ontology (GO) analysis, we carried out enrichment analysis for lipid structural attributes. Specifically, we developed an algorithm, termed LENA (i.e., lipid structural enrichment analysis), which determines the probability and odds ratio of whether a particular lipid molecular structure is over- or under-represented within a cluster (Figure 2C).

LENA revealed that the early fasting-related LL1 lipids are enriched in TAGs with polyunsaturated FA (PUFA) chains, as indicated by the FA attribute 18:2 and the 22:6-related backbone attributes 38:7, 40:7, 40:8, and 40:9 (Figures 2D and S2). Similarly, the late fasting-related LL2 lipids are also enriched in PUFA-containing TAGs, but with 20:4, 22:3, and 22:4 chains, as well as the 20:4-related backbone attributes 40:4 and 40:5. Notably, the FA chains enriched in LL2 can be synthesized by elongation and desaturation of 18:2 (i.e., linoleic acid), as well as 18:3 (i.e., linolenic acid), possibly explaining why LL2 shows a temporal delay and shallower incline relative to LL1 during fasting (Figure 2A).

For the food intake LL3 and postprandial-related LL4 lipids, we found two distinct patterns of structures (Figures 2D and S2). LL3 lipids are enriched in TAGs with the saturated and monounsaturated attributes 16:0, 34:1, 32:0, and 34:0, whereas LL4 lipids are specifically enriched in the membrane lipids PI, phosphatidic acid (PA), PC, and DMPE.

Together, these findings provide several insights into the diurnal remodeling of the liver lipidome. Specifically, during early fasting (i.e., LL1 lipids), where the TAG-NEFA cycle is elevated, we find that the liver produces TAGs with a high proportion of PUFA chains, especially 22:6 (i.e., docosahexaenoic acid) (Figures 2D and 2E). These 22:6-containing TAGs would likely be secreted as VLDL particles for transport back to the adipose tissue. With this notion in mind, it is interesting that the LL2 subset of TAGs, with 20:4 chains (i.e., arachidonic acid), accumulate in the liver for up to 2 h after onset of food intake, possibly related to a temporary attenuation of VLDL production and a switch to local storage in lipid droplets. Dysregulation of such switches could underpin the molecular defects that lead to metabolic disorders, such as fatty liver disease.

Our findings further show that the transition from fasting to feeding activates at least two consecutive lipid metabolic programs. The first is initiated upon food intake (within 1 h) and triggers synthesis of TAGs with saturated 16:0 and monounsaturated FA chains (i.e., LL3 lipids) (Figures 2D and 2E). These lipid structures are hallmarks of *de novo* lipogenesis and suggest that after food intake the liver absorbs dietary carbohydrates, such as glucose, and uses these for synthesis of saturated FA chains and glycerol-3-phosphate, which are then combined to produce TAG. After ~2 h, another metabolic program is launched (i.e., LL4 lipids), reflected in synthesis of the membrane lipids PI, DMPE, and PC via the intermediate PA (Figures 2D and 2E). Notably, all clustered DMPE and MMPE species are members of LL4 and LL3. Moreover, in LL4, these molecules primarily feature an 18:2 chain, whereas in LL3, they have a 22:6 chain. Together with the dynamics of LL4 and LL3 (Figure 2A), this finding strongly argues that the PE methylation pathway is progressively upregulated after food intake and across the postprandial state.

Profound diurnal oscillations in the blood plasma lipidome

To investigate the crosstalk between the liver and circulation, we determined the temporal coupling between the liver lipidome and correlated changes in the plasma lipidome. To do so, we carried out MS^{ALL} lipidomics of plasma across the two diurnal cycles (Figure 1A). We quantified (i.e., pmol/μL) 867 lipid molecules, belonging to 28 different lipid classes (Figure 3A; Table S2). 770 lipid molecules were identified at the molecular lipid species level and 97 lipids at the species level. Notably, we found six low-abundance DMPE species, including DMPE 16:0–18:2 and DMPE 16:0–22:6. By applying the same stringent statistical criteria used for the liver lipidome data, we found that 683 lipids (i.e., $p < 0.05$ and $r > 0.66$), equal to 79% of the plasma lipidome, display significant diurnal oscillations (Figure 3A). The majority of these oscillations are represented by glycerolipids (57%) and glycerophospholipids (18%) (Figure 3B).

Fuzzy c-means clustering of the oscillating plasma lipids (PLs) revealed four major timeline clusters: PL1, PL2, PL3, and PL4 (Figure 3C). Specifically, PL1 lipids increase during fasting, rapidly decrease upon feeding onset, then gradually increase during the remainder of the nocturnal period. PL2 lipids also increase during fasting, albeit with a shallower incline than that of the PL1 lipids, and rapidly decrease 1 h after feeding onset. PL3 lipids are rapidly reduced upon fasting onset, then rapidly increase following onset of feeding until they plateau in the middle of the night. PL4 lipids show a shallower decline compared with PL3 lipids during fasting, then increase after feeding onset, but with a ~1-h delay relative to PL3. Hierarchical clustering of these timelines revealed that the plasma lipidome transits through the same three periods as the liver lipidome (Figure 3D), arguing that oscillations in the circulation are also governed by adaptations to fasting, feeding, and the postprandial-like state.

Assessing lipid molecular signatures by LENA revealed that the early fasting-related PL1 lipids are primarily NEFA, lysophosphatidylcholine (LPC), and lysophosphatidylethanolamine (LPE) molecules with PUFA chains, especially 22:6 (Figures 3E and S3). Similarly, the late fasting-related PL2 lipids are also enriched in PUFA chains, but specifically 20:4 and 20:5, as well as cholesteryl esters (CEs). The food intake-related PL3 lipids are enriched in TAGs with saturated FA chains and also uniquely ether-linked PEs (i.e., PE O-), a lipid that is arguably among the least

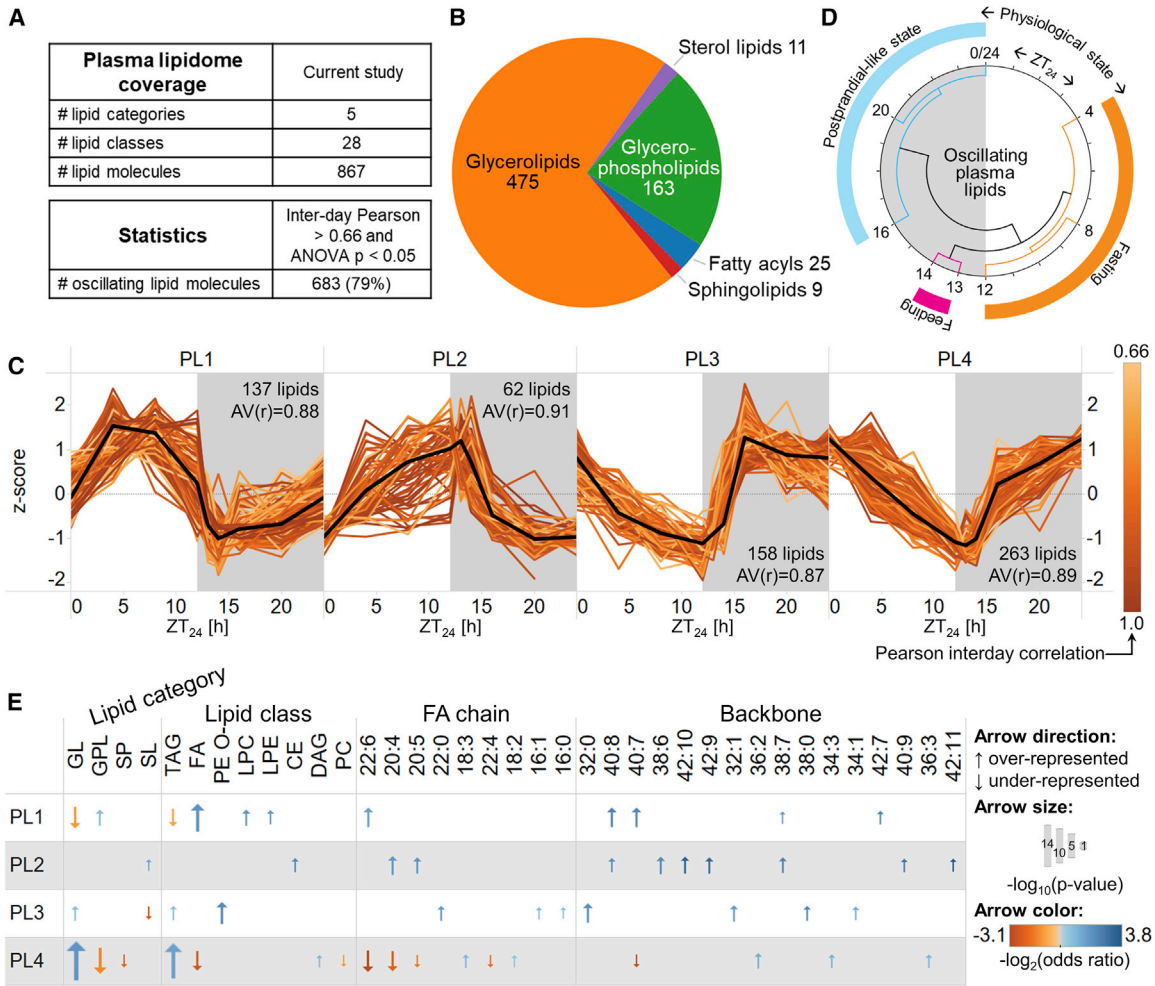

Figure 3. Oscillations in the plasma lipidome

(A) Plasma lipidome coverage and number of oscillating lipid molecules.

(B) Number of oscillating lipids distributed according to their lipid categories.

(C) Fuzzy c-means clustering of oscillating plasma lipids. Number of lipids and average Pearson correlation coefficient are denoted in individual plots.

(D) Hierarchical clustering of the plasma lipid timeline clusters.

(E) Over- and under-represented structural attributes in the plasma timeline clusters.

See also Figure S3.

understood in terms of circadian relevance. Finally, the postprandial-related PL4 lipids are enriched in TAGs and DAGs with 18:2 and 18:3 chains.

Together with the molecular signatures and similar dynamics of the liver timeline clusters (Figures 2A and 3C), these data suggest three modes of diurnal crosstalk among the liver, the circulation, and the intestine. First, the synchronous fasting-specific increase of 22:6-containing lipids in plasma PL1 and liver LL1 are due to activation of the TAG-NEFA cycle between adipose tissue and the liver. Second, the parallel food intake-specific increase in saturated and monounsaturated TAGs in plasma PL3 and liver LL3 results from *de novo* lipogenesis and secretion from the liver. Third, the parallel postprandial-specific increase in 18:2- and 18:3-containing TAGs in plasma PL4 and membrane lipids in liver LL4 is partly due to influx of dietary fat as intestinal-derived chylomicrons coupled to an efflux of membrane lipids from the liver, possibly to aid the turnover of the incoming chylomicrons. The fact that dietary fat contains high levels of 18:2 and 18:3 (Marcher et al., 2015) supports this notion. Further, there is a 3- to 4-h delay until chylomicrons reach the circulation (Bickerton et al., 2007), matching the timing of the increase in the postprandial-related PL4 lipids (Figure 3C).

Lipid metabolic crosstalk between the liver and circulation

To disentangle the molecular crosstalk between the liver and circulation, we used our lipidomics data to determine direct lipid metabolic couplings, defined as tight temporal correlation ($r > 0.66$) between identical lipid molecules or lipids with identical backbones in the liver and circulation (Figure 4A). Overall, we found that 169 lipids in the liver are directly coupled to an equivalent lipid in the circulation (Figure 4B). Among the three most tightly coupled

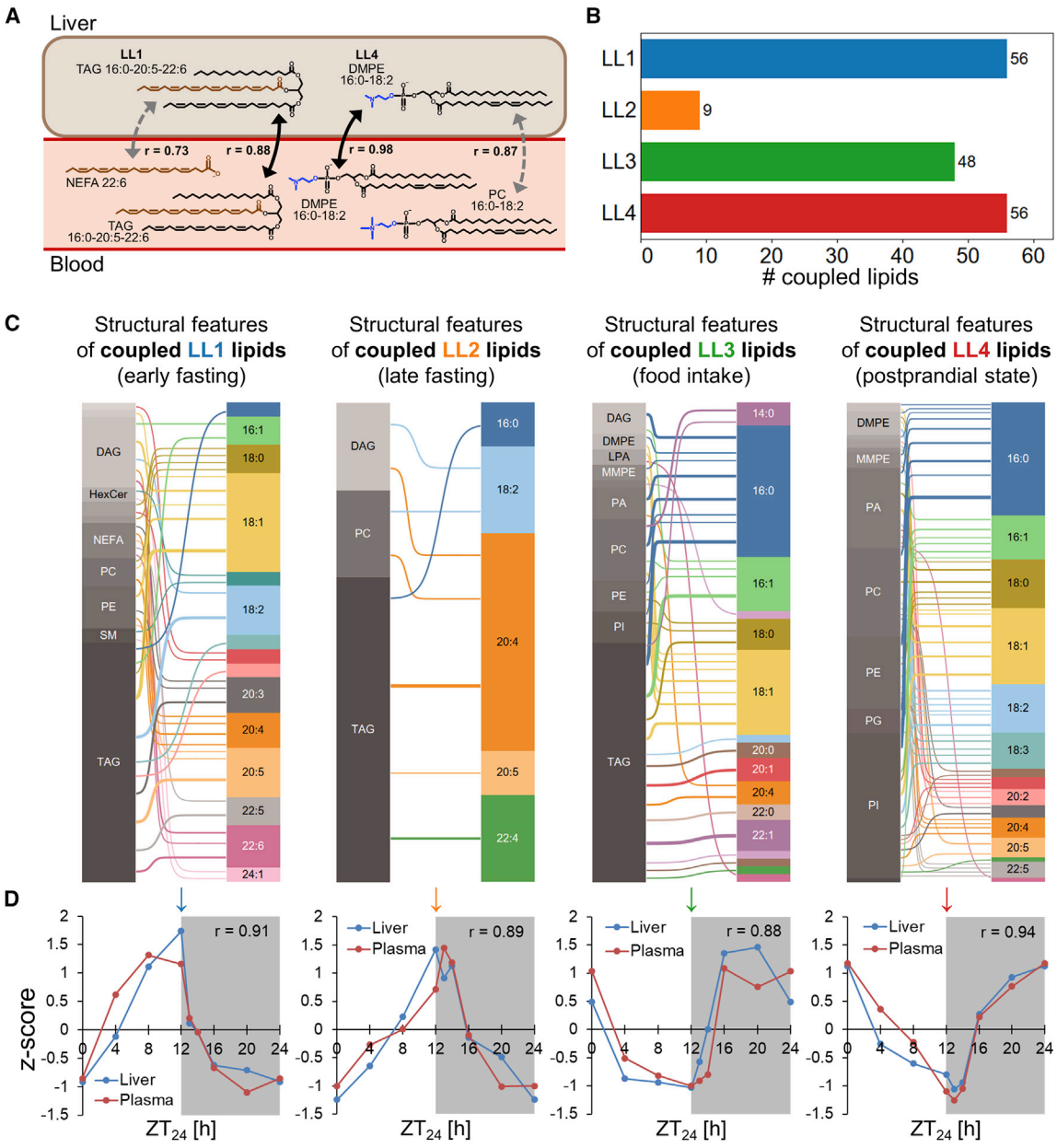

Figure 4. Diurnal regulation of lipid metabolic crosstalk between the liver and circulation

(A) Schematic of direct lipid metabolic couplings; defined as identical lipid molecules (black arrows) or lipid molecules with identical backbones (gray arrows) that are present in both liver and plasma and have a Pearson correlation coefficient (r) greater than 0.66.

(B) Number of lipids in LL1, LL2, LL3, and LL4 with a direct lipid metabolic coupling in the circulation.

(C) Sankey diagrams showing relationship between structural attributes from lipid classes and FA chains for coupled lipids in LL1, LL2, LL3, and LL4.

(D) Timelines of coupled LL1, LL2, LL3, and LL4 lipids in liver (blue) and counterparts in plasma (red).

See also Figure S4.

lipids, we found the putative Pemt-product DMPE 16:0–18:2 (r = 0.98), PI 18:0–18:2 (r = 0.96), and PE 16:0–18:1 (r = 0.94) (Figure S4A). Further analysis showed that 56, 9, 48, and 56 are lipids in LL1, LL2, LL3, and LL4, respectively (Figure 4B).

By examining structural attributes, we found that the coupled LL1 lipids feature a high proportion of 22:6- and other PUFA-containing TAGs and DAGs, as well as NEFA 22:6 itself (Figures 4A and 4C). Coupled LL2 lipids primarily include 20:4-containing TAGs and in cluster LL3 TAGs with 14:0, 16:0, 16:1, 18:0, and 18:1 chains. Notably, coupled LL4 lipids exclusively involve the membrane lipids PE, DMPE, PC, and PI. By inspecting the timelines of the coupled lipids, we unexpectedly found that the increase in the food-intake-related PLs are delayed by ~1 h relative to their LL3 counterparts in the liver, specifically after onset of

feeding (Figure 4D). In contrast, the timelines of coupled postprandial-related LL4 membrane lipids show no delay between the liver and plasma during the feeding period. For the early fasting LL1 lipids, there was a ~4-h delay relative to counterparts in plasma, specifically during fasting. Finally, coupled late fasting LL2 lipids and plasma counterparts uniquely accumulate in the liver and circulation for up to 2 h after onset of feeding.

Together, this analysis shows that the early fasting-specific increase of 22:6-containing TAGs in the liver and the plasma are indeed due to the concurrent increase of NEFA 22:6 in the circulation. Here, NEFA 22:6 is taken up by the liver, incorporated into TAGs, shown by the ~4-h delay, and secreted into the circulation as VLDL particles for return to adipose tissue. Notably, this tissue-specific 22:6 crosstalk is an unexplored hallmark of the TAG-NEFA cycle. Furthermore, our analysis also supports the hypothesis that the food intake-specific increase of saturated and monounsaturated TAGs in the circulation is indeed due to *de novo* lipogenesis in the liver followed by onset of secretion 1 h later, supposedly as VLDL particles. Finally, our results also provide evidence for direct postprandial-specific efflux of liver LL4 membrane lipids, including 18:2-containing DMPE. Notably, hepatic efflux of membrane lipids is inherent to the biogenesis of nascent HDL particles (Phillips, 2018). As such, it is plausible that the lipid efflux is coupled to production of HDL particles, and interestingly, that this is temporally coordinated with the influx of chylomicrons.

Diurnal regulation of the PE methylation pathway

Intrigued by our findings that MMPE and DMPE intermediates of the PE methylation pathways oscillate and show diurnal crosstalk between the liver and the circulation, we next examined their individual timelines in closer detail. Notably, the PE methyltransferase Pemt has been proposed to be responsible for 30% of PC synthesis in the liver, with the remainder derived from the CDP-choline pathway (DeLong et al., 1999). This occurs through a pathway where PE is methylated three times using S-adenosyl methionine (Figure 5A). Tracer studies have demonstrated that the PE methylation pathway *in vivo* produces primarily 22:6-containing PC molecules, albeit 18:2- and 20:4-containing PC species are also produced (Pynn et al., 2011). Furthermore, Pemt has been functionally linked to lipoprotein particle production, because its genetic deletion impairs secretion of Apob-containing VLDL particles in mice (Noga et al., 2002).

By examining the temporal profiles of MMPE and DMPE, in combination with corresponding PE substrates and PC products, we found that the PE methylation pathway gives rise to two distinct pools of PC molecules with different FA chains and patterns of oscillations in the circulation (Figures 5B and 5C). One pool comprises PC products with 18:2 chains, which are produced and secreted into the circulation primarily during the postprandial-like state and until the start of fasting (Figures 5B and S5A). This is further supported by similar dynamics of equivalent MMPE and DMPE substrates in liver and DMPE in the plasma. Counterintuitively, equivalent 18:2-containing PCs in the liver do not show the same oscillation, suggesting that their steady-state levels are maintained by the CDP-choline pathway. Importantly, these 18:2-containing lipids are all LL4-coupled postprandial-related membrane lipids that appear to be released to aid the production of HDL particles (Figure 4C).

The second pool comprises canonical PC products with 22:6 chains (Figures 5C and S5B). This pool is specifically elevated in the circulation during fasting and rapidly lowered upon onset of feeding. Again, counterintuitively, equivalent PCs in the liver do not oscillate, suggesting that their levels are also maintained by the CDP-choline pathway. Although the intermediate MMPEs and DMPEs do oscillate in the liver, their dynamics are opposite to that of their PC products in the circulation. This latter finding suggests that the 22:6-containing MMPEs and DMPEs temporarily accumulate in the liver after onset of feeding until they become fully methylated to PCs and then are secreted during the postprandial state and fasting. Notably, these 22:6-containing PC products are among the LL1-coupled early fasting lipids and could be released to cover the surface of the 22:6-rich VLDL particles destined for return to adipose tissue as part of the TAG-NEFA cycle.

PE methylation pathway enzymes are diurnally regulated

To address whether the diurnal regulation of the PE methylation pathway is governed by Pemt expression, and how this is linked to remodeling of lipid metabolism more broadly, we carried out label-free quantitative proteomics using 1D-LC-MS^2 analysis of liver samples and obtained timelines for 4,090 proteins (Figure S6A; Table S3). To increase the proteome coverage, we also analyzed pools of biological replicates using 2D-LC-MS^2 analysis and obtained timelines for 7,271 proteins. Combined, these timelines correspond to 7,511 distinct proteins (Figure S6B), of which 1,518 display a reproducible diurnal oscillation (i.e., $r > 0.66$, and either ANOVA $p < 0.05$ or >2-fold change in expression for proteins detected by 1D- or 2D-LC-MS^2, respectively) (Figure S6A). Fuzzy c-means clustering revealed that the oscillating liver proteins (LPs) cluster into three major timeline clusters: LP1, LP2, and LP3 (Figure S6C). Moreover, hierarchical clustering of these timelines revealed the same three temporal periods as the liver and plasma lipidomes (Figure S6D), demonstrating that diurnal remodeling of the liver proteome is also governed by primarily fasting-feeding cycles.

Specifically, we identified Pemt as a member of the LP1 cluster (Figure S6E) and found that its expression is characterized by temporary downregulation after food intake, followed by a progressive increase during the postprandial-like state and a gradual decrease across the fasting period (Figure 5D). This temporal dynamic is paralleled by four other LP1 members and auxiliary factors in the PE methylation pathway: Ahcyl2 and Bhmt2, involved in replenishment of S-adenosyl methionine, as well as Etnk2 and Chkb, which produce the intermediate phosphoethanolamine (Figure 5D). In addition, we found that Apob is an LP1 member and displays a similar temporal profile with characteristic downregulation immediately after food intake. Finally, to inspect the relationship between proteome remodeling and lipid oscillations, we performed hierarchical clustering of all timeline clusters (Figures S6F and S6G). This revealed that LP1 is specifically coupled to the postprandial-related liver LL4 ($r = 0.79$) and plasma PL4 ($r = 0.82$) lipids, which comprise the majority of oscillating MMPE and DMPE intermediates.

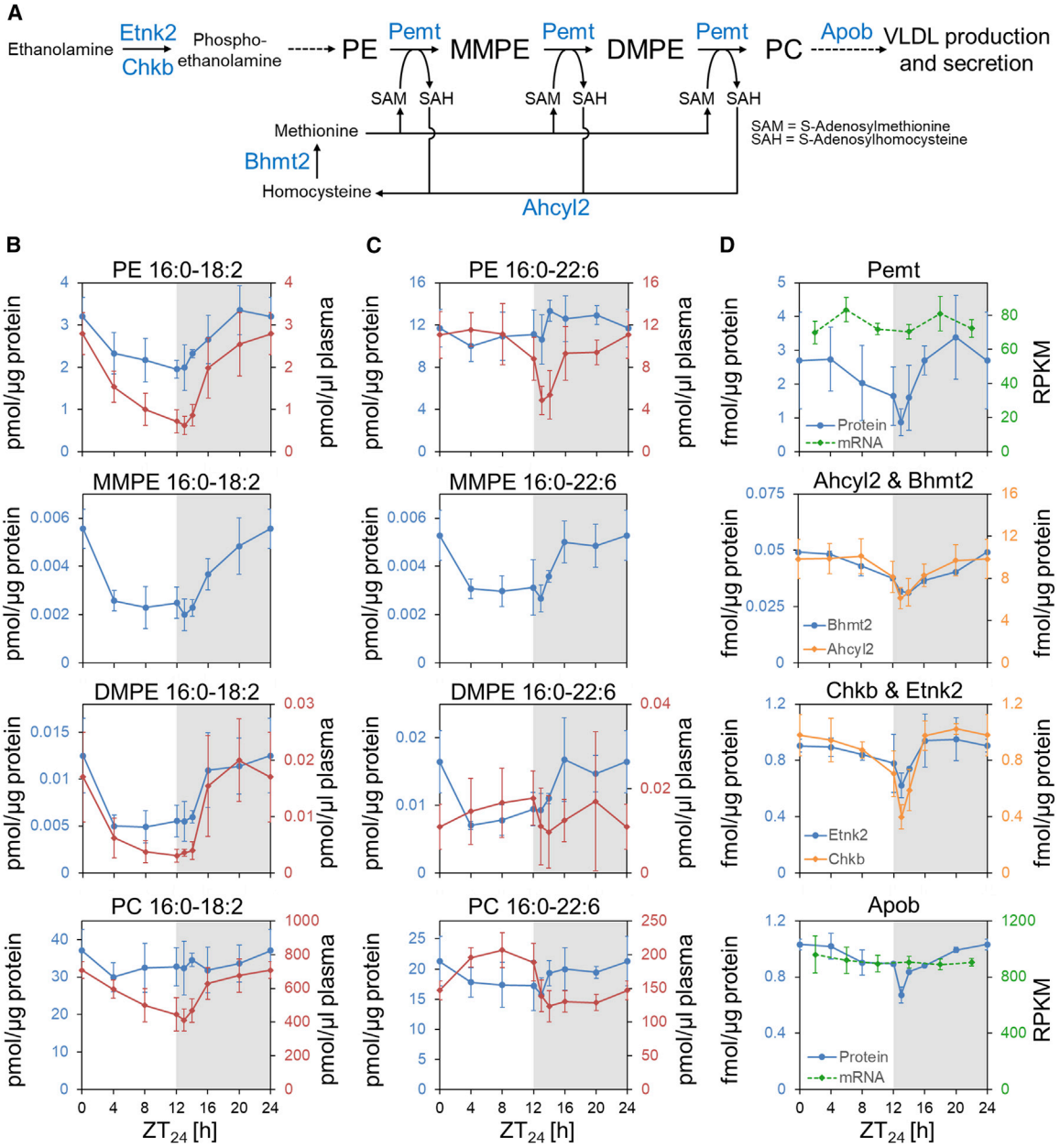

Figure 5. Diurnal regulation of the PE methylation pathway

(A) Schematic of the PE methylation pathway and proteins that are diurnally co-regulated (highlighted in blue).

(B) Timelines of PE, MMPE, DMPE, and PC molecules with a 16:0–18:2 backbone in liver (blue) and plasma (red).

(C) Timelines of PE, MMPE, DMPE, and PC molecules with a 16:0–22:6 backbone in liver (blue) and plasma (red).

(D) Timelines of liver proteins (blue and orange) involved in the PE methylation pathway and VLDL production. For comparative purposes, mRNA signals (Reads Per Kilobase Million (RPKM)) for Pemt and Apob are shown (green). The mRNA data are from Atger et al. (2015).

Data represent median ± 95% confidence interval for the median of five to six biological replicates.

See also Figures S5 and S6.

Overall, these results not only unequivocally demonstrate the PE methylation pathway is diurnally regulated at the protein expression level, but also suggest that the pathway is functionally coupled to secretion of Apob-containing VLDL particles across the diurnal cycle. More specifically, this suggests the hypotheses that plasma VLDL particles are reduced upon food intake, and that oscillating DMPE and PC molecules in the circulation are affected by genetic deletion of Pemt.

Lipid amount in VLDL and HDL particles is lowered upon food intake

To specifically test whether VLDL secretion is temporarily reduced following food intake, we carried out MS^{ALL} lipidomics

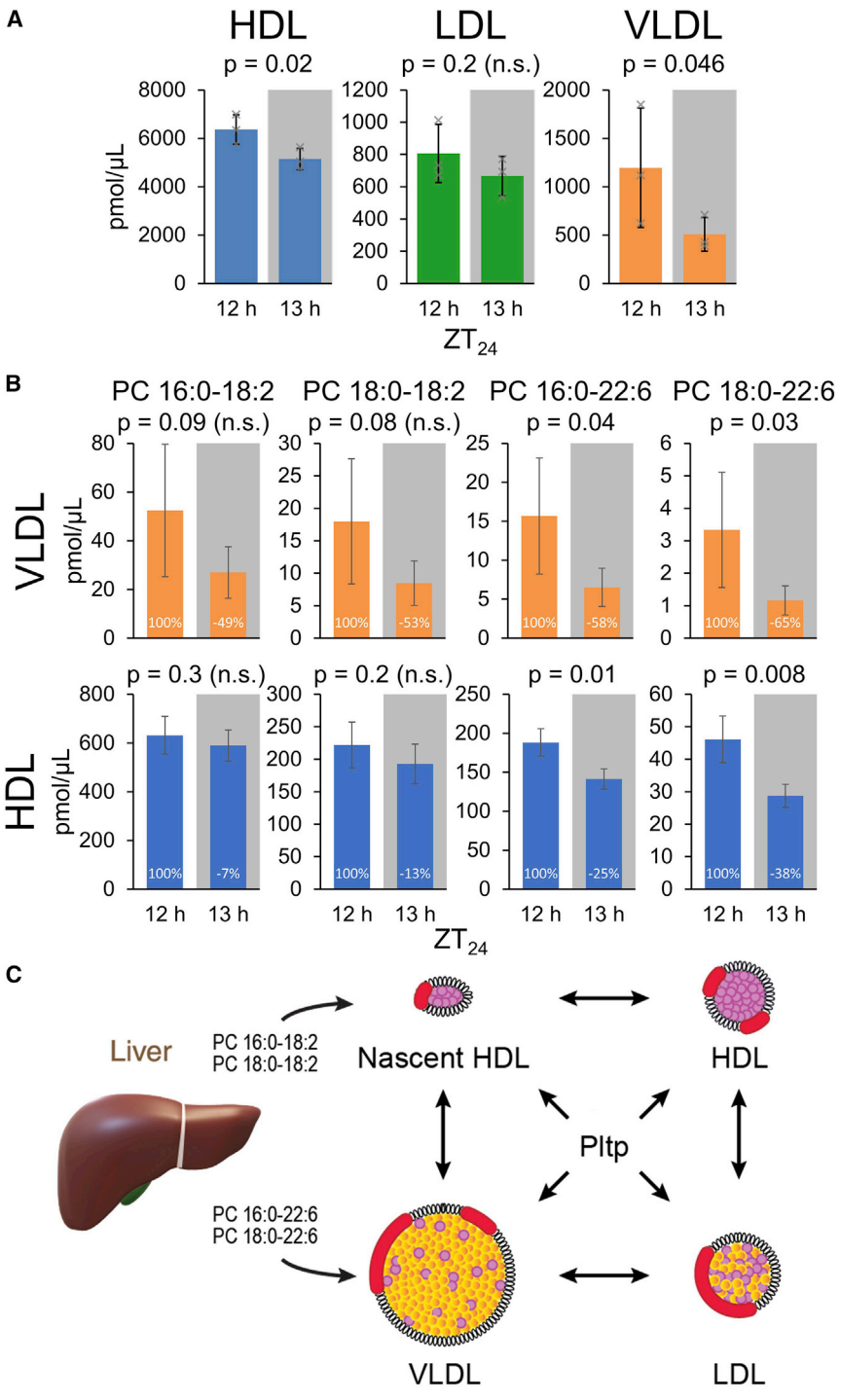

Figure 6. Reduction of VLDL in plasma after food intake

(A) Total lipid concentration associated with lipoprotein particles.

(B) Concentration of Pemt-relevant PC molecules associated with VLDL and HDL particles.

(C) Model of lipoprotein metabolism with focus on the putative roles of 22:6-containing PCs in VLDL secretion and 18:2-containing PCs in production of HDL particles. Phospholipid transfer protein (Pltp) mediates rapid transfer and equilibration of membrane lipids on the surfaces of lipoprotein particles. Model is adapted from Lusis and Pajukanta (2008).

Data represent mean ± SD (n = 3 biological replicates). Statistical significance was calculated using Student's t test.

See also Figure S7.

of all major lipoprotein particles. Specifically, we analyzed VLDL, low-density lipoprotein (LDL), and HDL particles after 12 h of fasting and after 1 h of feeding (i.e., ZT_{24} = 12 and 13 h, respectively) (Table S4). This analysis showed that each type of particle, independently of sampling time, has a distinct lipid class composition: VLDL is primarily composed of TAG; LDL contains similar amounts of TAG, CE, and PC; and HDL contains CE, PC, LPC, cholesterol, PE, and PI lipids (Figure S7). The analysis also confirmed that HDL followed by VLDL and LDL are the most abundant lipoprotein particles, as expected for mice (Figure 6A). Importantly, the higher levels of PI and PE specifically in HDL corroborate our notion that the liver secretes these LL4-specific membrane lipids (Figure 4C) for production of HDL particles.

Importantly, we uncovered that the total concentration of lipids associated with both VLDL and HDL particles are reduced by 57% and 19%, respectively, after 1 h of feeding (Figure 6A). In comparison, the total concentration of LDL-associated lipids is unchanged. This finding confirms our hypothesis that hepatic secretion of VLDL is temporally reduced upon food intake, possibly to mitigate a hyperlipidemic state due to the influx of chylomicrons. Interestingly, we also found a bipartite behavior of 18:2- and 22:6-containing PCs in the VLDL and HDL particles (Figure 6B). In these particles, 22:6-containing PCs become more reduced upon food intake as compared with the 18:2-containing PCs, and this reduction is more pronounced in VLDL as compared with HDL particles. This finding supports the notion of production and release of two pools of PC products, where the 22:6-containing PCs are coupled to VLDL secretion and PCs with 18:2 chains are important for HDL production (Figure 6C).

Pemt$^{-/-}$ mice produce high levels of MMPE and DMPE

Finally, to ascertain whether Pemt is responsible for the oscillation of circulating 18:2- and 22:6-containing DMPEs and PCs, we carried out a lipidomics analysis of plasma from Pemt$^{-/-}$

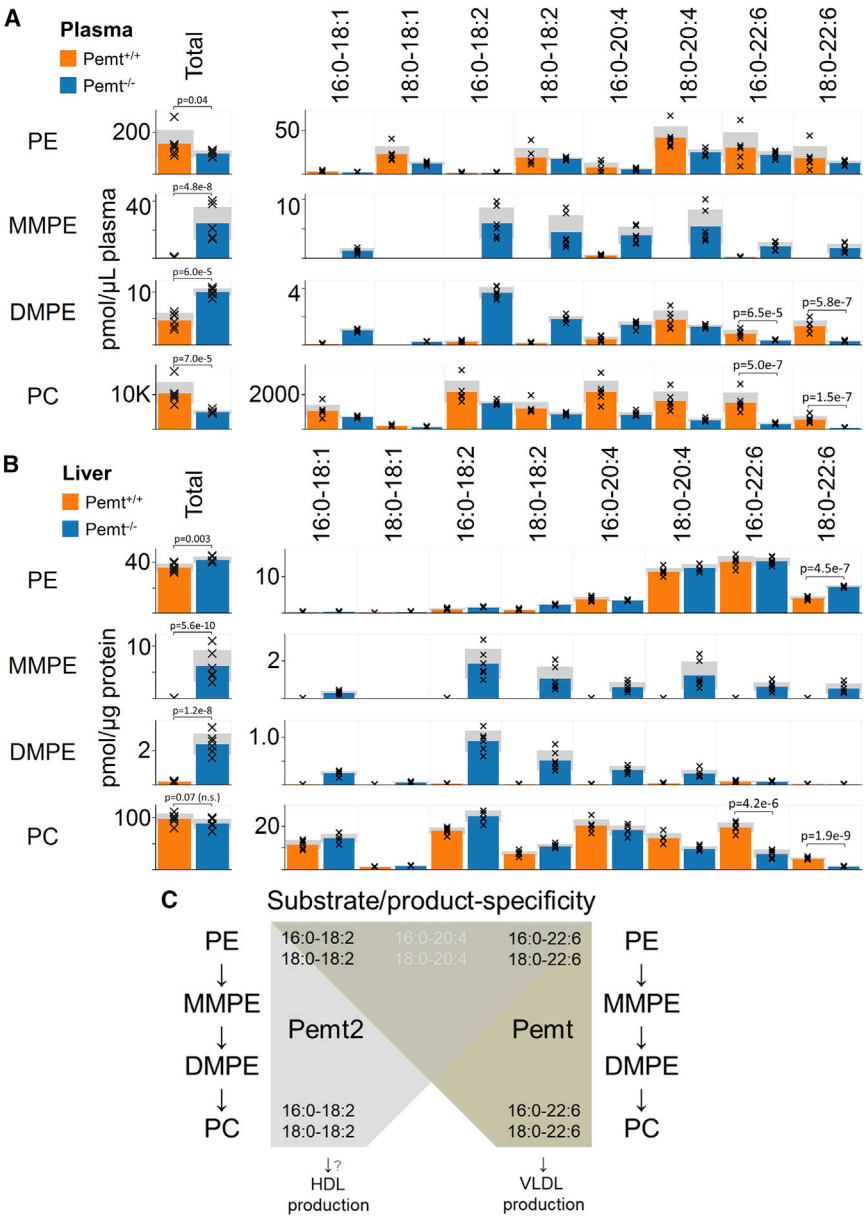

Figure 7. Unexpected production of MMPE and DMPE lipids in Pemt$^{-/-}$ mice

(A) Total levels and concentrations of individual PE, MMPE, DMPE, and PC lipids in plasma from Pemt$^{-/-}$ and wild-type mice.

(B) Total levels and abundances of individual PE, MMPE, DMPE, and PC lipids in liver from Pemt$^{-/-}$ and wild-type mice.

(C) Model of enzymatic properties and functions of Pemt and the putative PE methyltransferase Pemt2.

Data represent mean ± SD (gray box) and cross individual measurements (n = 6 biological replicates). Statistical significance was calculated using Student's t test.

mice fasted for 12 h (Table S5). This verified that the fasting-specific increase of 22:6-containing DMPEs and PCs is indeed due to Pemt, because its genetic ablation reduced their levels by up to 7-fold as compared with wild-type mice (Figure 7A). Much to our surprise, however, we also observed that the total levels of MMPE and DMPE are 42- and 2-fold higher in plasma of Pemt$^{-/-}$ mice. Specifically, we found that these increases are primarily due to MMPE and DMPE molecules with 18:2 chains and, to a lesser extent, 20:4 and 22:6 chains (Figure 7A).

It is truly mysterious why Pemt$^{-/-}$ mice have elevated levels of MMPE and DMPE lipids in their circulation, which they should not produce according to our knowledge of the PE methylation pathway. We therefore also examined the molecular composition of MMPE and DMPE in the liver of Pemt$^{-/-}$ mice. This revealed that the total levels of MMPE and DMPE are 136- and 14-fold higher, respectively, as compared with wild-type mice (Figure 7B; Table S6). Moreover, we again found that MMPEs and DMPEs primarily feature 18:2 chains, albeit Pemt$^{-/-}$ mice also produce MMPEs with 22:6, and this FA chain is even less abundant in the DMPE class. Our analysis also showed that the composition of PEs is largely unchanged in Pemt$^{-/-}$ mice, with the exception of an elevated PE 18:0–22:6 level. In addition, we observed an increase in 18:2-containing PCs, as well as a specific reduction in canonical 22:6-containing PCs, confirming that Pemt is genuinely ablated in the knockout mice.

Taken together, these findings provide two fundamental insights. First, they verify that oscillations in circulating 22:6-containing DMPE and PC, and the corresponding MMPE and DMPE species in liver, are due to Pemt activity. Second, they indicate that there is another pathway synthesizing MMPE and DMPE, hinting at a so far undiscovered PE methyltransferase. The activity of this putative enzyme (which we term Pemt2) is also diurnally regulated. This pathway primarily produces MMPE, DMPE, and PC species with 18:2 chains (Figure 7C). Furthermore, our different data suggest that the canonical Pemt-related products with 22:6 chains are functionally linked to VLDL secretion, whereas the putative Pemt2-related products with 18:2 chains are coupled to HDL production.

DISCUSSION

We comprehensively characterized molecular oscillations in the mouse liver and circulation using a framework that uniquely captures responses to fasting-feeding transitions and circadian rhythms. Overall, our data reveal that 50%, 79%, and 20% of the liver lipidome, plasma lipidome, and liver proteome,

respectively, exhibit diurnal oscillations. Importantly, our liver lipidome data confirm previous findings that numerous TAGs and PCs display oscillations (Adamovich et al., 2014) and reveal, due to its broader coverage, that these oscillations extend to a multitude of other lipid molecules belonging to several other lipid classes. By time-series clustering and lipid structure enrichment analysis, as well as integration of plasma lipidome and liver proteome data, we uncover that the majority of oscillations are entrained by physiological adaptations to fasting, food intake, and a postprandial-like state, and that this gives rise to three modes of diurnal interorgan crosstalk. These modes are characterized by a fasting-specific cycling of lipids with 22:6 chains between adipose tissue and the liver, a feeding-specific increase in the production and secretion of saturated TAGs from the liver, and a postprandial-specific increase in the biosynthesis and efflux of membrane lipids from the liver. Altogether, our longitudinal multi-omics data provide a valuable resource for the study of diurnal regulation of whole-body lipid metabolism and demonstrate the utility of in-depth lipid molecular timeline profiling to decipher complex metabolic processes.

Besides uncovering unexpected global patterns of metabolic regulation and crosstalk, we also demonstrate that our resource leverages insights into the regulation of distinct metabolic pathways. Specifically, we discover that the hepatic PE methylation pathway is diurnally regulated, and that this gives rise to two pools of oscillating PC molecules in the circulation. Specifically, we find evidence that canonical PCs with 22:6 chains are produced by Pemt and coupled to VLDL secretion during fasting, and that 18:2-containing PCs appear to be made by a so far undiscovered PE methyltransferase and are coupled to production of HDL particles (Figure 7C). This latter finding, corroborated by the specific production of 18:2-containing MMPE and DMPE species in Pemt$^{-/-}$ mice, as well as an overlooked residual PE methylation activity in the knockout mice (Walkey et al., 1997), might be a first step in a major revision of our understanding of mammalian lipid biochemistry. These conclusions could also help to elucidate why Pemt$^{-/-}$ mice are protected from diet-induced atherosclerosis (van der Veen et al., 2017). Notably, for the last three decades Pemt has been considered the only PE methyltransferase in mammals (Cui et al., 1993), whereas yeast have two enzymes: Cho2 and Opi3. Here, Cho2 can only produce MMPE from PE, whereas Opi3, which is homologous to Pemt, can catalyze all three methylations to produce PC directly from PE (Bilgin et al., 2011). Thus, it is likely that the yeast *CHO2* gene and the putative Pemt2 gene are evolutionarily related, and that the latter has evolved to also be able to convert MMPE to DMPE and possibly DMPE to PC. It will be exciting in the future to identify the putative Pemt2 gene and establish its molecular functions.

Finally, we note that lipid molecular timeline profiling provides an avenue for more accurate mapping of metabolic health that goes far beyond comparison of lipid levels from only fasted animals. In fact, our data demonstrate that a multitude of lipids and proteins fluctuate with different dynamics across the 12-h fasting period. Hence single-time-point comparisons could potentially fail to uncover physiologically relevant oscillations and be misleading. Obviously, the use of lipid molecular timelines will increase the usage of animals and demand that the lipidomics technology can cope with the increased sample throughput. The latter is not a limitation, as our study shows, and one can foresee that time-series experiments with ~50 mice per cohort, as well as storage of tissues in biobanks that can be shared among the scientific community, would in the long run reduce the total number of animals used for biomedical studies. Lastly, we believe that lipid molecular timelines will be highly useful in personalized medicine, with the potential to improve the diagnosis of metabolic health. Related to this, our resource also reveals oscillations in ceramides prognostic of cardiovascular mortality in humans (Tarasov et al., 2014) (Figure S4B), suggesting that these biomarkers are signatures of the liver's inability to remodel metabolic processes across the diurnal cycle.

In summary, our study provides a high-quality resource comprising molecular oscillations in the liver and circulation of mice, highlights that lipid oscillations are primarily governed by physiological adaptations to fasting-feeding cycles, demonstrates that the enzymatic activities of Pemt, as well as another putative PE methyltransferase, are diurnally regulated, and lays the groundwork for the use of lipid molecular timeline profiling in the study of whole-body lipid metabolism and homeostasis.

STAR★METHODS

Detailed methods are provided in the online version of this paper and include the following:

- KEY RESOURCES TABLE
- RESOURCE AVAILABILITY
  - Lead contact
  - Materials availability
  - Data and code availability
- EXPERIMENTAL MODEL AND SUBJECT DETAILS
  - Animal studies
- METHOD DETAILS
  - Lipid extraction of liver and plasma samples
  - Lipoprotein separation by FPLC
  - Lipid extraction of lipoprotein particles
  - Lipidomics by high-resolution MS^{ALL} analysis
  - Sample preparation for proteomics analysis
  - Proteomics by 1D-LC-MS^2 analysis
  - Proteomics by 2D LC-MS^2 analysis
- QUANTIFICATION AND STATISTICAL ANALYSIS
  - Lipid nomenclature
  - Lipid abundances from mass spectrometric data
  - Statistical analysis and clustering of lipidomics data
  - Bioinformatics analysis of lipidomics data
  - Peptide identification
  - Protein quantification from 1D-LC-MS^2 data
  - Protein quantification from 2D-LC-MS^2 data
  - Statistical analysis and clustering of proteomics data
  - Bioinformatics analysis of proteomics data

SUPPLEMENTAL INFORMATION

Supplemental Information can be found online at https://doi.org/10.1016/j.celrep.2021.108710.

ACKNOWLEDGMENTS

We thank Alba Diz-Muñoz, Sabbi Lall, Nils Hoffmann, and Robert Ahrends for constructive comments and Peter Højrup for amino acid analysis. This research was supported by the VILLUM Foundation (VKR023439 to C.S.E.), the VILLUM Center for Bioanalytical Sciences (VKR023179 to O.N.J. and C.S.E.), and the Lundbeckfonden (R44-A4342 and R54-A5858 to C.S.E.). The research leading to these results has received funding from the European Union Seventh Framework Programme (FP7-2007-2013) under grant agreement "HEALTH-F2-2013-602222 (Athero-Flux)" (O.N.J. and C.S.E.).

AUTHOR CONTRIBUTIONS

C.S.E., D.E.V., D.N., G.L., J.E., M.H., N.J.F., and R.R.S. conceived and designed the study. C.S.E., D.N., L.S.B., M.H., R.R.S., and S.B.S. conducted the experiments. C.S.E. and R.F. analyzed data. C.S.E. and R.W.K. wrote the paper. C.S.E., D.E.V., G.L., J.E., M.H., N.J.F., O.N.J., and R.W.K. supervised the project.

DECLARATION OF INTERESTS

The authors declare no competing interests.

Received: September 4, 2020
Revised: October 29, 2020
Accepted: January 8, 2021
Published: February 2, 2021

REFERENCES

Adamovich, Y., Rousso-Noori, L., Zwighaft, Z., Neufeld-Cohen, A., Golik, M., Kraut-Cohen, J., Wang, M., Han, X., and Asher, G. (2014). Circadian clocks and feeding time regulate the oscillations and levels of hepatic triglycerides. Cell Metab. *19*, 319–330.

Almeida, R., Pauling, J.K., Sokol, E., Hannibal-Bach, H.K., and Ejsing, C.S. (2015). Comprehensive lipidome analysis by shotgun lipidomics on a hybrid quadrupole-orbitrap-linear ion trap mass spectrometer. J. Am. Soc. Mass Spectrom. *26*, 133–148.

Atger, F., Gobet, C., Marquis, J., Martin, E., Wang, J., Weger, B., Lefebvre, G., Descombes, P., Naef, F., and Gachon, F. (2015). Circadian and feeding rhythms differentially affect rhythmic mRNA transcription and translation in mouse liver. Proc. Natl. Acad. Sci. USA *112*, E6579–E6588.

Bickerton, A.S., Roberts, R., Fielding, B.A., Hodson, L., Blaak, E.E., Wagenmakers, A.J., Gilbert, M., Karpe, F., and Frayn, K.N. (2007). Preferential uptake of dietary Fatty acids in adipose tissue and muscle in the postprandial period. Diabetes *56*, 168–176.

Bilgin, M., Markgraf, D.F., Duchoslav, E., Knudsen, J., Jensen, O.N., de Kroon, A.I., and Ejsing, C.S. (2011). Quantitative profiling of PE, MMPE, DMPE, and PC lipid species by multiple precursor ion scanning: a tool for monitoring PE metabolism. Biochim. Biophys. Acta *1811*, 1081–1089.

Bligh, E.G., and Dyer, W.J. (1959). A rapid method of total lipid extraction and purification. Can. J. Biochem. Physiol. *37*, 911–917.

Bray, M.S., Ratcliffe, W.F., Grenett, M.H., Brewer, R.A., Gamble, K.L., and Young, M.E. (2013). Quantitative analysis of light-phase restricted feeding reveals metabolic dyssynchrony in mice. Int. J. Obes. *37*, 843–852.

Casanovas, A., Sprenger, R.R., Tarasov, K., Ruckerbauer, D.E., Hannibal-Bach, H.K., Zanghellini, J., Jensen, O.N., and Ejsing, C.S. (2015). Quantitative analysis of proteome and lipidome dynamics reveals functional regulation of global lipid metabolism. Chem. Biol. *22*, 412–425.

Chaix, A., Lin, T., Le, H.D., Chang, M.W., and Panda, S. (2019). Time-Restricted Feeding Prevents Obesity and Metabolic Syndrome in Mice Lacking a Circadian Clock. Cell Metab. *29*, 303–319.e4.

Chua, E.C., Shui, G., Lee, I.T., Lau, P., Tan, L.C., Yeo, S.C., Lam, B.D., Bulchand, S., Summers, S.A., Puvanendran, K., et al. (2013). Extensive diversity in circadian regulation of plasma lipids and evidence for different circadian metabolic phenotypes in humans. Proc. Natl. Acad. Sci. USA *110*, 14468–14473.

Cui, Z., Vance, J.E., Chen, M.H., Voelker, D.R., and Vance, D.E. (1993). Cloning and expression of a novel phosphatidylethanolamine N-methyltransferase. A specific biochemical and cytological marker for a unique membrane fraction in rat liver. J. Biol. Chem. *268*, 16655–16663.

Dallmann, R., Viola, A.U., Tarokh, L., Cajochen, C., and Brown, S.A. (2012). The human circadian metabolome. Proc. Natl. Acad. Sci. USA *109*, 2625–2629.

DeLong, C.J., Shen, Y.J., Thomas, M.J., and Cui, Z. (1999). Molecular distinction of phosphatidylcholine synthesis between the CDP-choline pathway and phosphatidylethanolamine methylation pathway. J. Biol. Chem. *274*, 29683–29688.

Eckel-Mahan, K.L., Patel, V.R., de Mateo, S., Orozco-Solis, R., Ceglia, N.J., Sahar, S., Dilag-Penilla, S.A., Dyar, K.A., Baldi, P., and Sassone-Corsi, P. (2013). Reprogramming of the circadian clock by nutritional challenge. Cell *155*, 1464–1478.

Ellis, S.R., Paine, M.R.L., Eijkel, G.B., Pauling, J.K., Husen, P., Jervelund, M.W., Hermansson, M., Ejsing, C.S., and Heeren, R.M.A. (2018). Automated, parallel mass spectrometry imaging and structural identification of lipids. Nat. Methods *15*, 515–518.

Fahy, E., Subramaniam, S., Murphy, R.C., Nishijima, M., Raetz, C.R., Shimizu, T., Spener, F., van Meer, G., Wakelam, M.J., and Dennis, E.A. (2009). Update of the LIPID MAPS comprehensive classification system for lipids. J. Lipid Res. *50* (*Suppl*), S9–S14.

Frayn, K.N. (2002). Adipose tissue as a buffer for daily lipid flux. Diabetologia *45*, 1201–1210.

Freyre, C.A.C., Rauher, P.C., Ejsing, C.S., and Klemm, R.W. (2019). MIGA2 Links Mitochondria, the ER, and Lipid Droplets and Promotes De Novo Lipogenesis in Adipocytes. Mol. Cell *76*, 811–825.e14.

Gallego, S.F., Sprenger, R.R., Neess, D., Pauling, J.K., Færgeman, N.J., and Ejsing, C.S. (2017). Quantitative lipidomics reveals age-dependent perturbations of whole-body lipid metabolism in ACBP deficient mice. Biochim. Biophys. Acta Mol. Cell Biol. Lipids *1862*, 145–155.

Gallego, S.F., Højlund, K., and Ejsing, C.S. (2018). Easy, Fast, and Reproducible Quantification of Cholesterol and Other Lipids in Human Plasma by Combined High Resolution MSX and FTMS Analysis. J. Am. Soc. Mass Spectrom. *29*, 34–41.

Hatori, M., Vollmers, C., Zarrinpar, A., DiTacchio, L., Bushong, E.A., Gill, S., Leblanc, M., Chaix, A., Joens, M., Fitzpatrick, J.A., et al. (2012). Time-restricted feeding without reducing caloric intake prevents metabolic diseases in mice fed a high-fat diet. Cell Metab. *15*, 848–860.

Held, N.M., Wefers, J., van Weeghel, M., Daemen, S., Hansen, J., Vaz, F.M., van Moorsel, D., Hesselink, M.K.C., Houtkooper, R.H., and Schrauwen, P. (2020). Skeletal muscle in healthy humans exhibits a day-night rhythm in lipid metabolism. Mol. Metab. *37*, 100989.

Højrup, P. (2015). Analysis of Peptides and Conjugates by Amino Acid Analysis. Methods Mol. Biol. *1348*, 65–76.

Hughes, M.E., Abruzzi, K.C., Allada, R., Anafi, R., Arpat, A.B., Asher, G., Baldi, P., de Bekker, C., Bell-Pedersen, D., Blau, J., et al. (2017). Guidelines for Genome-Scale Analysis of Biological Rhythms. J. Biol. Rhythms *32*, 380–393.

Husen, P., Tarasov, K., Katafiasz, M., Sokol, E., Vogt, J., Baumgart, J., Nitsch, R., Ekroos, K., and Ejsing, C.S. (2013). Analysis of lipid experiments (ALEX): a software framework for analysis of high-resolution shotgun lipidomics data. PLoS ONE *8*, e79736.

Isherwood, C.M., Van der Veen, D.R., Johnston, J.D., and Skene, D.J. (2017). Twenty-four-hour rhythmicity of circulating metabolites: effect of body mass and type 2 diabetes. FASEB J. *31*, 5557–5567.

Käll, L., Canterbury, J.D., Weston, J., Noble, W.S., and MacCoss, M.J. (2007). Semi-supervised learning for peptide identification from shotgun proteomics datasets. Nat. Methods *4*, 923–925.

Liebisch, G., Vizcaíno, J.A., Köfeler, H., Trötzmüller, M., Griffiths, W.J., Schmitz, G., Spener, F., and Wakelam, M.J. (2013). Shorthand notation for lipid structures derived from mass spectrometry. J. Lipid Res. *54*, 1523–1530.

Loizides-Mangold, U., Perrin, L., Vandereycken, B., Betts, J.A., Walhin, J.P., Templeman, I., Chanon, S., Weger, B.D., Durand, C., Robert, M., et al. (2017). Lipidomics reveals diurnal lipid oscillations in human skeletal muscle persisting in cellular myotubes cultured in vitro. Proc. Natl. Acad. Sci. USA *114*, E8565–E8574.

Lusis, A.J., and Pajukanta, P. (2008). A treasure trove for lipoprotein biology. Nat. Genet. *40*, 129–130.

Marcher, A.B., Loft, A., Nielsen, R., Vihervaara, T., Madsen, J.G., Sysi-Aho, M., Ekroos, K., and Mandrup, S. (2015). RNA-Seq and Mass-Spectrometry-Based Lipidomics Reveal Extensive Changes of Glycerolipid Pathways in Brown Adipose Tissue in Response to Cold. Cell Rep. *13*, 2000–2013.

Metsalu, T., and Vilo, J. (2015). ClustVis: a web tool for visualizing clustering of multivariate data using Principal Component Analysis and heatmap. Nucleic Acids Res. *43* (*W1*), W566–W570.

Minami, Y., Kasukawa, T., Kakazu, Y., Iigo, M., Sugimoto, M., Ikeda, S., Yasui, A., van der Horst, G.T., Soga, T., and Ueda, H.R. (2009). Measurement of internal body time by blood metabolomics. Proc. Natl. Acad. Sci. USA *106*, 9890–9895.

Noga, A.A., Zhao, Y., and Vance, D.E. (2002). An unexpected requirement for phosphatidylethanolamine N-methyltransferase in the secretion of very low density lipoproteins. J. Biol. Chem. *277*, 42358–42365.

Panda, S. (2019). The arrival of circadian medicine. Nat. Rev. Endocrinol. *15*, 67–69.

Pauling, J.K., Hermansson, M., Hartler, J., Christiansen, K., Gallego, S.F., Peng, B., Ahrends, R., and Ejsing, C.S. (2017). Proposal for a common nomenclature for fragment ions in mass spectra of lipids. PLoS ONE *12*, e0188394.

Phillips, M.C. (2018). Is ABCA1 a lipid transfer protein? J. Lipid Res. *59*, 749–763.

Pynn, C.J., Henderson, N.G., Clark, H., Koster, G., Bernhard, W., and Postle, A.D. (2011). Specificity and rate of human and mouse liver and plasma phosphatidylcholine synthesis analyzed in vivo. J. Lipid Res. *52*, 399–407.

Reddy, A.B., and O'Neill, J.S. (2010). Healthy clocks, healthy body, healthy mind. Trends Cell Biol. *20*, 36–44.

Reshef, L., Olswang, Y., Cassuto, H., Blum, B., Croniger, C.M., Kalhan, S.C., Tilghman, S.M., and Hanson, R.W. (2003). Glyceroneogenesis and the triglyceride/fatty acid cycle. J. Biol. Chem. *278*, 30413–30416.

Sampaio, J.L., Gerl, M.J., Klose, C., Ejsing, C.S., Beug, H., Simons, K., and Shevchenko, A. (2011). Membrane lipidome of an epithelial cell line. Proc. Natl. Acad. Sci. USA *108*, 1903–1907.

Saran, A.R., Dave, S., and Zarrinpar, A. (2020). Circadian Rhythms in the Pathogenesis and Treatment of Fatty Liver Disease. Gastroenterology *158*, 1948–1966.e1.

Schwämmle, V., and Jensen, O.N. (2018). VSClust: feature-based variance-sensitive clustering of omics data. Bioinformatics *34*, 2965–2972.

Silva, J.C., Gorenstein, M.V., Li, G.Z., Vissers, J.P., and Geromanos, S.J. (2006). Absolute quantification of proteins by LCMSE: a virtue of parallel MS acquisition. Mol. Cell. Proteomics *5*, 144–156.

Soccio, R.E., Chen, E.R., and Lazar, M.A. (2014). Thiazolidinediones and the promise of insulin sensitization in type 2 diabetes. Cell Metab. *20*, 573–591.

Spivak, M., Weston, J., Bottou, L., Käll, L., and Noble, W.S. (2009). Improvements to the percolator algorithm for Peptide identification from shotgun proteomics data sets. J. Proteome Res. *8*, 3737–3745.

Tarasov, K., Ekroos, K., Suoniemi, M., Kauhanen, D., Sylvänne, T., Hurme, R., Gouni-Berthold, I., Berthold, H.K., Kleber, M.E., Laaksonen, R., and März, W. (2014). Molecular lipids identify cardiovascular risk and are efficiently lowered by simvastatin and PCSK9 deficiency. J. Clin. Endocrinol. Metab. *99*, E45–E52.

van der Veen, J.N., Kennelly, J.P., Wan, S., Vance, J.E., Vance, D.E., and Jacobs, R.L. (2017). The critical role of phosphatidylcholine and phosphatidylethanolamine metabolism in health and disease. Biochim. Biophys. Acta Biomembr. *1859* (*9 Pt B*), 1558–1572.

Walkey, C.J., Donohue, L.R., Bronson, R., Agellon, L.B., and Vance, D.E. (1997). Disruption of the murine gene encoding phosphatidylethanolamine N-methyltransferase. Proc. Natl. Acad. Sci. USA *94*, 12880–12885.

Wallace, M., and Metallo, C.M. (2020). Tracing insights into de novo lipogenesis in liver and adipose tissues. Semin. Cell Dev. Biol. *108*, 65–71.

Wang, G., Wu, W.W., Zhang, Z., Masilamani, S., and Shen, R.F. (2009). Decoy methods for assessing false positives and false discovery rates in shotgun proteomics. Anal. Chem. *81*, 146–159.

Wiesner, P., Leidl, K., Boettcher, A., Schmitz, G., and Liebisch, G. (2009). Lipid profiling of FPLC-separated lipoprotein fractions by electrospray ionization tandem mass spectrometry. J. Lipid Res. *50*, 574–585.

STAR★METHODS

KEY RESOURCES TABLE

REAGENT or RESOURCE	SOURCE	IDENTIFIER
Chemicals, peptides, and recombinant proteins		
Altromin 1324	Brogaarden	Cat# 1324
Mouse Diet	Bio-Serv	Cat# F3282
K3E micro tubes	Sarstedt	Cat# NC9414041
Water (LCMS grade)	VWR	Cat# 83645.320
Ammonium formate	Fluka	Cat# 17843
Methanol (LCMS grade)	Biosolve	Cat# 13687802BS
Chloroform (HPLC grade)	Rathburn	Cat# RH1009
Phosphate buffered saline (PBS)	Sigma-Aldrich	Cat# P3813
Ethylenediamine tetraacetic acid disodium salt dihydrate (EDTA)	Carl Roth	Cat# 8043
2-propanol (LCMS grade)	Biosolve	Cat# 16267802BS
Methylamine	Sigma-Aldrich	Cat# 65568
Ammonium acetate	Sigma-Aldrich	Cat# 73594
Sodium deoxycholate (SDC)	Sigma-Aldrich	Cat# 30968
Tris(2-carboxyethyl)phosphine	Sigma-Aldrich	Cat# 646547
2-chloroacetamide	Fluka	Cat# 22788
Triethylammonium bicarbonate	Fluka	Cat# 17902
Trypsin	Promega	Cat# V5111
Dimethyl sulfoxide (DMSO)	Biosolve	Cat# 4470602
Ethyl acetate	Sigma-Aldrich	Cat# 650528
Trifluoroacetic acid	Biosolve	Cat# 202341A8BS
Hi3 *E. coli* ClpB standard	Waters Corporation	Cat# 186006012
Acetonitrile	Biosolve	Cat# 1204101BS
Formic acid	Biosolve	Cat# 69141A8BS
CE 10:0	Sigma-Aldrich	Cat# C4633
CE 19:0	Avanti Polar Lipids	Cat# LM4000
Cer 18:1;2/17:0	Avanti Polar Lipids	Cat# 860517
Cer 18:1;2/17:0;1	Avanti Polar Lipids	Cat# 860517P
Cholesterol(+$^{2}H_{7}$)	Avanti Polar Lipids	Cat# 700041P
CL 14:0/14:0/14:0/14:0	Avanti Polar Lipids	Cat# 7103320
DAG(+$^{2}H_{5}$) 17:0/17:0	Avanti Polar Lipids	Cat# 850149P
TAG(+$^{2}H_{5}$) 17:0/17:1/17:0	Avanti Polar Lipids	Cat# 110544P
LPA O-16:0	Avanti Polar Lipids	Cat# 110683
PA 17:0/20:4	Avanti Polar Lipids	Cat# LM1402
LPS 17:1	Avanti Polar Lipids	Cat# 800740X
PS 17:0/20:4	Avanti Polar Lipids	Cat# LM1302
PS 17:0/14:1	Avanti Polar Lipids	Cat# LM1304
LPE O-16:0	Avanti Polar Lipids	Cat# 110703
PE O-20:0/20:0	Avanti Polar Lipids	Cat# 999985C
LPC O-17:0	Avanti Polar Lipids	Cat# 878101P
LPC 16:0(+$^{2}H_{3}$)	Larodan AB	Cat# 71-2826
PC 16:0(+$^{2}H_{3}$)/16:0(+$^{2}H_{3}$)	Larodan AB	Cat# 71-3726
LPI 17:1	Avanti Polar Lipids	Cat# 850103P
PI 17:0/20:4	Avanti Polar Lipids	Cat# LM1502
PG 17:0/14:1	Avanti Polar Lipids	Cat# LM1204

(*Continued on next page*)

Continued

REAGENT or RESOURCE	SOURCE	IDENTIFIER
CL 14:0/14:0/14:0/14:0	Avanti Polar Lipids	Cat# 7103320
SM 18:1;2/17:0	Avanti Polar Lipids	Cat# 860585
GlcCer 18:1;2/12:0	Avanti Polar Lipids	Cat# 860543
GM3 18:1;2/18:0(+$^{2}H_{5}$)	Avanti Polar Lipids	Cat# 860073
NEFA 17:0(+$^{2}H_{3}$)	Larodan AB	Cat# 71-1703
SPLASH® LIPIDOMIX® Mass Spec Standard	Avanti Polar Lipids	Cat# 330707
Deposited data		
Proteomics data	This paper	Deposited to the ProteomeXchange Consortium via the PRIDE partner repository with the dataset identifier PXD008944.
Experimental models: organisms/strains		
Mus musculus / C57BL/6JBomTac	Taconic Biosciences	Cat# B6JBOM-M
Mus musculus / Pemt$^{-/-}$	Walkey et al., 1997	N/A
Software and algorithms		
ALEX^{123}	Ellis et al., 2018; Husen et al., 2013; Pauling et al., 2017	http://mslipidomics.info/contents/?page_id=525
SAS 9.4	SAS Institute Inc.	N/A
Tableau Desktop 2019.1.3	Tableau Software, Inc.	N/A
VSClust	Schwämmle and Jensen, 2018	http://computproteomics.bmb.sdu.dk/Apps/VSClust
ClustVis	Metsalu and Vilo, 2015	https://biit.cs.ut.ee/clustvis/
Venny 2.1	N/A	https://bioinfogp.cnb.csic.es/tools/venny/index.html
Microsoft Excel 2019	Microsoft	N/A
Proteome Discoverer v.2.1.1.21	Thermo Fisher Scientific	N/A
Mascot server, version 2.3	Matrix Science	N/A
Progenesis QI for proteomics v2.0	Nonlinear Dynamics / Waters	N/A
Percolator algorithm	Käll et al., 2007	N/A
Other		
TriVersa NanoMate	Advion Biosciences	N/A
Orbitrap Fusion Tribrid mass spectrometer	Thermo Fisher Scientific	N/A
Bioruptor UCD-200 system	Diagenode	N/A
Dionex Ultimate 3000 nano UPLC system	Thermo Fisher Scientific	N/A
Symmetry C18 trap column (180 μm x 20 mm; 5 μm particle size)	Waters Corporation	Cat# 186007500
BEH C18 column (75 μm x 250 mm; 1.7 μm particle size)	Waters Corporation	Cat# 186007484
XBridge BEH C18 (300 μm x 50 mm, 5 μm particle size)	Waters Corporation	Cat# 186003682
Biochrom 30 amino acid analyzer	Biochrom	Cat# 80-6000-50
Pharmacia Smart FPLC System	GE Healthcare Europe	N/A
T 10 basic ULTRA-TURRAX®	IKA	Cat# 0003737000
Superose 6 PC 3.2/30 column	Sigma-Aldrich	Cat# GE17-0673-01

RESOURCE AVAILABILITY

Lead contact

Further information and requests for resources and reagents should be directed to and will be fulfilled by the Lead Contact, Christer S. Ejsing (cse@bmb.sdu.dk).

Materials availability

All reagents generated in this study are available from the Lead Contact without restriction.

Data and code availability

Lipidomics data on liver, plasma, lipoprotein particles, plasma and liver from Pemt$^{-/-}$ mice are provided in Tables S1, S2, S4, S5, and S6, respectively. Proteomics data is provided in Table S3. Raw LC-MS-based proteomics data is deposited in the ProteomeXchange Consortium via the PRIDE partner repository with the dataset identifier: PXD008944.

EXPERIMENTAL MODEL AND SUBJECT DETAILS

Animal studies

Male wild-type C57BL/6JBomTac mice (7 weeks old) were obtained from Taconic Biosciences (Lille Skensved, Denmark) and were allowed to adapt to the housing in the Biomedical Laboratory (University of Southern Denmark) for 1 week prior to random assignment into experimental cohorts. The mice were housed under standard conditions with controlled humidity (55%) and temperature (22 ± 3°C), 12 h light/dark cycle (light on at 6 am (ZT_{24} = 0) and light off at 6 pm (ZT_{24} = 12)) and fed a standard rodent laboratory diet (Altromin 1324, Brogaarden) and water *ad libitum*. Two days prior to the study, the mice were entrained to nighttime-restricted feeding with access to food only during the nocturnal period (6 pm (ZT_{24} = 12) to 6 am (ZT_{24} = 24/0)) and free access to water at all times. For the time-restricted feeding study, the mice were allowed access to food only during the nocturnal period and three mice were euthanized at the time points, ZT_{24} = 0, 4, 8, 12, 13, 14, 16 and 20 h, and across two diurnal cycles. Before euthanasia mice were anesthetized and blood was sampled by retro-orbital bleeding into K3E micro tubes (Sarstedt). Plasma was separated by centrifugation (3000 g, 15 min, 4°C) and snap frozen in liquid nitrogen. Mice were perfused with 10 mL 155 mM ammonium acetate by cardiac puncture and the liver was dissected, snap frozen in liquid nitrogen and stored at −80°C until further processing. The study was conducted in accordance with the Danish law on Animal Experiments (LBK no. 1306 – 23/11/2007, amendments § 1 nr. 612 – 14/06/2011) and approved by the Danish Animal Experiment Inspectorate.

Male Pemt$^{+/+}$ and Pemt$^{-/-}$ mice (backcrossed into C57BL/6 for seven generations; and 8-10 weeks old) were housed under standard conditions and fed a semisynthetic diet (#F3282, Bio-Serv; 60 kcal% fat from lard) for 2 weeks. The mice were fasted for 12 h before sacrifice by exsanguination (cardiac puncture). Liver and plasma were collected, snap-frozen in liquid nitrogen, and stored at −80°C until further processing. The study was approved by the University of Alberta's Institutional Animal Care Committee in accordance with guidelines of the Canadian Council on Animal Care.

METHOD DETAILS

Lipid extraction of liver and plasma samples

Liver tissue was homogenized at 80°C in 155 mM ammonium acetate using an ULTRA-TURRAX (IKA). The homogenate was briefly incubated in a water bath for 2 minutes at 80°C, and vortexed before taking an aliquot for total protein determination by amino acid analysis (Højrup, 2015), after which the sample was frozen in liquid nitrogen and stored at −80°C. These liver homogenates were fast-thawed in an 80°C water bath and aliquots corresponding to 25 μg total protein were subjected to two-step lipid extraction at 4°C, as previously described (Gallego et al., 2017; Sampaio et al., 2011). Briefly, tissue homogenates were diluted with 155 mM ammonium formate to a final volume of 200 μL and spiked with an internal lipid standard mixture containing cholesteryl ester (CE) 19:0, cholesterol(+$^2H_7$), TAG 17:0/17:1/17:0(+$^2H_5$), diacylglycerol (DAG) 17:0/17:0(+$^2H_5$), lysophosphatidic acid (LPA) O-16:0, phosphatidic acid (PA) 17:0/20:4, lysophosphatidylserine (LPS) 17:1, phosphatidylserine (PS) 17:0/20:4, lysophosphatidylethanolamine (LPE) O-16:0, phosphatidylethanolamine (PE) O-20:0/O-20:0, lysophosphatidylcholine (LPC) O-17:0, phosphatidylcholine (PC) 16:0(+$^2H_3$)/16:0(+$^2H_3$), lysophosphatidylinositol (LPI) 17:1, phosphatidylinositol (PI) 17:0/20:4, phosphatidylglycerol (PG) 17:0/14:1, cardiolipin (CL) 14:0/14:0/14:0/14:0, ceramide (Cer) 18:1;2/17:0, sphingomyelin (SM) 18:1;2/17:0, and glucosylceramide (GlcCer) 18:1;2/12:0 (we note that it is preferable to use stable isotope-labeled standards for every lipid class and molecule, and not odd-chain analogs as these can be of low abundance in biological matrices). Subsequently 990 μL of chloroform/methanol (10:1, v/v) was added to the samples, which were mixed for 120 min at 1400 rpm. Samples were centrifuged for 2 min at 1000 g to facilitate phase separation. The lower organic phase was collected and vacuum evaporated. The remaining aqueous phase was re-extracted with 990 μL of chloroform/methanol (2:1, v/v) by mixing for 90 min at 1400 rpm. Samples were centrifuged for 2 min at 1000 g, the lower organic phase was collected and vacuum evaporated.

Plasma samples (10 μL) were diluted with 155 mM ammonium formate to a final volume of 200 μL and spiked with an internal lipid standard mixture containing CE 10:0, cholesterol(+$^2H_7$), TAG 17:0/17:1/17:0(+$^2H_5$), DAG 17:0/17:0(+$^2H_5$), PS 17:0/14:1, PI 17:0/20:4, LPE O-16:0, PE O-20:0/O-20:0, LPC 16:0(+$^2H_3$), PC 16:0/16:0(+$^2H_6$), PG 17:0/14:1, Cer 18:1;2/17:0 and SM 18:1;2/17:0. Lipid extraction of plasma samples was carried out as described above for liver.

Lipoprotein separation by FPLC

VLDL, LDL and HDL particles were isolated from 12 h fasted mice (ZT_{24} = 12 h) or 1 h refed mice (ZT_{24} = 13 h) by fast performance liquid chromatography (FPLC), as previously described (Wiesner et al., 2009). In brief, a Pharmacia Smart FPLC System equipped

with a Superose 6 PC 3.2/30 column (GE Healthcare Europe GmbH) was preconditioned with phosphate buffered saline (PBS; Sigma-Aldrich) containing 1 mM ethylenediamine tetraacetic acid disodium (EDTA; Carl Roth). After loading 50 μL plasma the system was run with a constant flow of 40 μL/min, and fractionation was started after 18 min with 80 μL per fraction. Fractions 3-6 containing VLDL particles were pooled (total volume 320 μL), fractions 7-11 containing LDL particles were pooled (total volume 400 μL), and fractions 12-17 containing HDL particles and albumin were pooled (total volume 480 μL). The pooled fractions were snap-frozen in liquid nitrogen and stored at −80°C until further analyses.

Lipid extraction of lipoprotein particles

Lipid extraction of the collected lipoprotein particles was performed according to Bligh and Dyer (1959). In brief, 120 μL of each lipoprotein particle fraction (i.e., VLDL, LDL and HDL) was mixed with 155 mM ammonium formate to give a total volume of 200 μL and thereafter spiked with an internal lipid standard mixture containing SPLASH LIPIDOMIX (i.e., PC 15:0/18:1(+$^2H_7$), PE 15:0/18:1(+$^2H_7$), PS 15:0/18:1(+$^2H_7$), PG 15:0/18:1(+$^2H_7$), PI 15:0/18:1(+$^2H_7$), PA 15:0/18:1(+$^2H_7$), LPC 18:1(+$^2H_7$), LPE 18:1(+$^2H_7$), CE 18:1(+$^2H_7$), MAG 18:1(+$^2H_7$), DAG 15:0/18:1(+$^2H_7$), TAG 15:0/18:1(+$^2H_7$)/15:0, SM 18:1;2/18:1(+$^2H_9$) and cholesterol(+$^2H_7$)) plus LPI 17:1, LPS 17:1, Cer 18:1;2/17:0;1, GM3 18:1;2/18:0(+$^2H_5$), GlcCer 18:1;2/12:0, LPA O-16:0 and NEFA 17:0(+$^2H_3$). 750 μL of chloroform/methanol (1:2, v/v) was added to these samples and they were then mixed for 20 min at 2000 rpm, followed by addition of 250 μL chloroform and 250 μL 155 mM ammonium formate, and mixed for another 20 min at 2000 rpm. The samples where then centrifuged for 3 min at 3000 g to facilitate phase separation and the lower organic phase was collected. The remaining upper phase was re-extracted with 500 μL chloroform for 20 min and then centrifuged for 3 min at 3000 g. The lower organic phase was combined with the previously collected lower phase and vacuum evaporated.

Lipidomics by high-resolution MS^{ALL} analysis

Lipid extracts were dissolved in chloroform/methanol (1:2, v/v) and subjected to mass spectrometric analysis using a high-resolution Orbitrap Fusion Tribrid (Thermo Fisher Scientific) equipped with a TriVersa NanoMate (Advion Biosciences), as previously described (Almeida et al., 2015; Gallego et al., 2017). Briefly, lipid extracts were loaded in 96-well plates, mixed with 13.3 mM ammonium formate in 2-propanol for positive ion mode analysis, and 1.33 mM ammonium formate in 2-propanol or 0.01% methylamine in methanol for negative ion mode analysis. Samples were infused using a back pressure of 1.25 psi and ionization voltage of ± 0.95 kV. FTMS data were recorded using a max injection time of 100 ms, automated gain control at 2e5, 2 microscans and a target resolution of 500,000 (FWHM at *m/z* 200). $FTMS^2$ data were acquired using max injection time of 100 ms, automated gain control at 5e4, 1 microscan and a target resolution of 30,000. All FTMS data were acquired using an ion transfer tube temperature of 275°C.

Sample preparation for proteomics analysis

Liver tissue was homogenized at 80°C in 155 mM ammonium acetate. The homogenate was briefly incubated in a water bath for 2 minutes at 80°C and vortexed before taking an aliquot for total protein determination by amino acid analysis (Højrup, 2015), after which the sample was frozen in liquid nitrogen and stored at −80°C. These liver homogenates were fast-thawed in an 80°C water bath and aliquots corresponding to 100 μg total protein (based on the amino acid analysis) were taken and mixed with pre-heated protein lysis, reduction and alkylation buffer to a final volume of 100 μL with a concentration of 1% sodium deoxycholate, 10 mM tris(2-carboxyethyl)phosphine, 40 mM 2-chloroacetamide and 50 mM triethylammonium bicarbonate. Samples were then sonicated using a Bioruptor UCD-200 system (Diagenode) at 4°C for 10 minutes with 30 s on/off cycles. Then 2 μg of trypsin was added to each 100 μg protein in the solution followed by incubation at 37°C for 10 hours. Subsequently, dimethyl sulfoxide was added to a final concentration of 10% followed by 400 μL ethyl acetate and trifluoroacetic acid (0.25% final concentration) and immediate vortexing for 5 min at 10°C. Samples were centrifuged for 10 min at 14,000 g at 10°C, after which the peptide containing lower phase was transferred to a new tube and stored at −80°C until LC-MS^2 analysis.

Proteomics by 1D-LC-MS^2 analysis

Tryptic peptides (2 μg) were mixed with 50 fmol of the synthetic *E. coli* ClpB internal protein standard (Waters Corporation) to enable estimation of absolute protein abundances by label-free quantification. Peptide separation was performed with a Dionex Ultimate 3000 nano UPLC system (Thermo Fisher Scientific) fitted with a Symmetry C18 trap column (180 μm x 20 mm; 5 μm particle size; Waters) and an BEH C18 analytical column (75 μm x 250 mm; 1.7 μm particle size; Waters). Peptides were trapped for 2 min at 15 μL/min with 0.1% trifluoroacetic acid and separated at 350 nL/min using a 70 min gradient of 2%–35% acetonitrile with 0.1% formic acid, followed by column washing at 85% acetonitrile and re-equilibration with 80 min of total data collection. Eluting peptides were ionized at 1.7 kV using a TriVersa NanoMate (Advion Biosciences) as nanoelectrospray ion source coupled to an Orbitrap Fusion Tribrid mass spectrometer (Thermo Fischer Scientific) with the source capillary temperature set at 275°C. Full MS scans (*m/z* 350-1500) were acquired at target resolution 120,000 (at *m/z* 200) with wide window quadrupole isolation turned on. Full scan target was 5e5 with a maximum fill time of 100 ms and all data were acquired in profile mode. For tandem MS the instrument was run in top speed mode with maximum 5 s cycles selecting precursors above 5e4 intensity with charge state 2-6. Targets were isolated at ± 0.35 Da using the quadrupole followed by HCD fragmentation with normalized collision energy of 30% and rapid scan MS analysis in the ion trap. For MS^2 analysis the AGC target value was 1e4 with a maximum fill time of 35 ms and using the all-parallelizable-time option. To increase the overall numbers of identifications, a method variant was used alternating between each sample, using a maximum fill

time of 100 ms combined with the only-single-charge-state-per-precursor option. For both methods the dynamic exclusion time was set to 45 s with a ± 10 ppm tolerance.

Proteomics by 2D LC-MS^2 analysis

Equal amounts of tryptic peptides from each replicate per time point were pooled together (5 μg in total) and 100 fmol of the synthetic *E. coli* ClpB internal protein standard was added (Waters Corporation). Peptides were analyzed by online 2D-RP-RP (high pH reversed phase/low pH reversed phase) LC-MS^2, as previously described (Casanovas et al., 2015). In short, peptides were first trapped using an XBridge BEH C18 column (300 μm x 50 mm; 5 μm particle size; Waters) at 2 μL/min with 3% acetonitrile in 20 mM ammonium formate (pH 10). To generate ten fractions, discrete two-minute steps at 2 μL/min of respectively 8%, 11.5%, 13%, 15%, 16.5%, 18%, 20%, 21.5%, 24% and 50% acetonitrile were used. Eluting fractions were online acidified and diluted 10-fold with 0.1% trifluoroacetic acid in water at 20 μL/min and trapped on a Symmetry C18 trapping column. Each fraction was separated with an BEH C18 analytical column at 350 nL/min using a 30 min gradient of 6%–28% acetonitrile with 0.1% formic acid and column washing at 85% acetonitrile. For each subsequent fraction the gradient start and end-points were increased with 1% with a total data collection time of 35 minutes per fraction. The total analysis time for one sample with ten fractions was about 7 hours. Eluting peptides were ionized at 1.7 kV using the TriVersa NanoMate coupled to the Orbitrap Fusion Tribrid mass spectrometer. MS and MS^2 acquisitions were identical to the method described for 1D-LC-MS^2 analysis, except for using top speed mode with maximum 1.5 s cycles, dynamic exclusion time set to 20 s with a ± 5 ppm tolerance and not applying a second alternating method.

QUANTIFICATION AND STATISTICAL ANALYSIS

Lipid nomenclature

Lipid categories and lipid classes are denoted by their category and class abbreviations, respectively (Fahy et al., 2009; Liebisch et al., 2013; Pauling et al., 2017). For lipids reported at the "species-level," the combined number of carbons and double bonds in the FA chains is indicated after the lipid class abbreviation. For example, "PE 38:4" denotes a PE lipid with 38 carbons and 4 double bonds spread across both individual FA chains. For lipids reported at the "molecular species-level" (i.e., identification of individual FA chain compositions), individual FAs are indicated in the format of 'total number of carbons:number of double bonds', with individual FAs separated by a dash. For example, "PE 16:0-22:6" indicates a PE lipid containing a 16:0 and a 22:6 FA chain. For ether lipids, ether-bound hydrocarbon chains are preceded with an "O" indicating either 1-O-alkyl ether or 1-O-alkenyl ether (plasmalogen) linkage. For example, PE O-18:1/20:4 is a PE O- lipid with a 20:4 FA chain and an 18-carbon ether-linked chain with one double bond. The double bond could be either that of a 1-O-alkenyl ether or positioned along the remainder of the FA chain as a 1-O-alkyl ether. We note that *sn*- positions and double-bond positions of individual FAs cannot be accurately resolved by the applied lipidomics technology.

Lipid abundances from mass spectrometric data

Identification and quantification of lipid molecules was done using the ALEX^{123} framework and auxiliary data processing pipelines in SAS 9.4 (SAS Institute); as previously described (Almeida et al., 2015; Ellis et al., 2018; Husen et al., 2013; Pauling et al., 2017). Briefly, lipid molecules detected by full-scan FTMS were identified using a maximum *m/z* tolerance of ± 0.0040 amu, corrected for potential ^{13}C isotope interference, required to have a relative detection frequency of 0.66 (equivalent to being detected in 66% of all biological replicates for a given sample group) and reported at the "species-level." Lipid fragment ions detected by FTMS^2 were identified using a maximum *m/z* tolerance of ± 0.0065 amu, required to have a relative detection frequency of 0.50 (equivalent to being detected in 50% of all biological replicates in a given sample group) and reported as "molecular lipid species-specific fragments" (MLF) or "lipid class-specific fragments" (LCF) (Ellis et al., 2018; Pauling et al., 2017). For high-confidence identification of lipids reported at the sum-composition-level (e.g., PC 34:1), at least one confirmatory LCF detected by FTMS^2 was required. For high-confidence identification of molecular lipid species identified by detection of MLFs, the following criteria were set: (i) the asymmetric molecular lipid species must be detected by at least two complementary pairs of MLFs (except for protonated PE O- species that do not release abundant complementary MLFs); (ii) the molecular lipid species must have an ALEX^{123} score > 0.5 (calculated as the number of detected MLFs relative to the total number of MLFs available in the ALEX^{123} database) or an ALEX^{123} score $\leq$ 0.5 but with detection of > 2 MLFs (with the exception that protonated PE O- species could be detected by at least 2 MLFs); and (iii) confirmation by detection of the corresponding lipid molecule at the species-level by full-scan FTMS. Identified lipid molecules were quantified by normalizing their measured intensities to that of respective internal lipid standards, subsequent multiplication by the amount of the respective lipid standard and normalization to the extracted sample amount (i.e., μg liver protein or μL plasma). Visual inspection of data quality and lipidome features was done using Tableau Desktop (Tableau Software).

Statistical analysis and clustering of lipidomics data

The inter-day Pearson correlation coefficient was calculated for averaged timelines of individual lipid molecules using SAS 9.4 (SAS Institute). Furthermore, statistical analysis by ANOVA was also carried out using SAS 9.4. Lipid timelines with p values less than 0.05 and an inter-day Pearson correlation greater than 0.66 were considered statistically significant. For comparative visualization and clustering analysis, individual lipid abundances were log2 transformed and converted to z-scores. Statistically significant lipid

timelines were analyzed by fuzzy c-means clustering using VSClust (Schwämmle and Jensen, 2018). Hierarchical clustering of centroid timeline clusters was carried out using ClustVis (Metsalu and Vilo, 2015) with Euclidean clustering distance and the Ward's clustering method. Statistical analysis of lipid data shown in bar graphs is done using log2 transformation and by Student's t test in Excel (Microsoft).

Analysis of whether omitting the time points ZT_{24} = 13 and 14 h significantly biases the true temporal dynamics of lipid timelines (Figures 1E and 1F) was carried out in three steps using SAS 9.4. First, a linear regression between the time points ZT_{24} = 12 and 16 h was determined for individual lipid molecules. This regression was used to estimate *apparent* lipid abundances at the time points ZT_{24} = 13 and 14 h. Second, one-sample Student's t testing was carried out between the *measured* and *apparent* lipid abundances for both the time points ZT_{24} = 13 and 14 h. A p value < 0.05 was considered significant (i.e., that a *measured (true)* lipid abundance is significantly different compared to the estimated *apparent* lipid abundance). Third, lipids with significant differences at time points ZT_{24} = 13 or/and 14 h were classified as having timelines that are significantly biased (by not including the time points ZT_{24} = 13 and 14 h; and therefore, specifically entrained by fasting-feeding cycles.

Bioinformatics analysis of lipidomics data

Lipid structural ENrichment Analysis (LENA) was carried out using SAS 9.4 and is essentially based on the principle of contingency table analysis and Fisher's exact test. In brief, for lipid molecules within a given cluster as well as that of all detected lipid molecules (i.e., background list) LENA determines four different lipid structural attributes: "lipid category," "lipid class," "backbone" and "FA chain" (where the latter requires the lipid molecule to be identified at the "molecular species-level") (Figure 2C). LENA next computes the (relative) occurrence of the different lipid structural attributes for lipids in the cluster as well as that among all detected lipid molecules. Using Fisher's exact test, LENA subsequently computes the probability of the observed relative occurrence of a particular lipid structural feature happening by random chance, as well as the odds-ratio (observed relative occurrence divided by the relative background occurrence).

Analysis of direct lipid metabolic couplings between lipid molecules in the liver and the plasma was carried out using SAS 9.4. In short, pairwise Pearson correlation coefficients were determined for all individual lipid timelines in liver and plasma. Next, the data was filtered to retain only pairwise liver-plasma Pearson correlation coefficients greater than 0.66; and this data was further filtered to only shortlist identical lipid molecules (i.e., DMPE 16:0-18:2 in liver and DMPE 16:0-18:2 in plasma) or lipid molecules with identical backbones (e.g., DMPE 16:0-22:6 in liver and PC 16:0-22:6 in plasma, where "16:0-22:6" is the backbone). Next, the shortlisted lipid molecules were grouped based on the name of their liver lipid (LL) timeline cluster and the occurrence of the lipid structural attributes "lipid class" and "FA chain" for each cluster were determined. Finally, Sankey diagrams were generated in Tableau Desktop using the relative occurrence of the structural attributes and their molecular relationship.

Peptide identification

Fragmentation spectra were searched using the search engine Mascot against a FASTA formatted database containing all canonical and isoform UniProtKB entries for *Mus musculus*, version 0513 with common contaminants and protein quantitation standards added (81029 entries in total). The search was facilitated through the Proteome Discoverer software (v2.1, Thermo Scientific) using the following parameters: trypsin, maximum 2 missed cleavages, cysteine carbamidomethylation as a fixed modification and acetylation of protein N-terminal, and oxidation of methionine as dynamic modifications. Search tolerances were set to ± 10 ppm for peptide precursors and ± 0.35 Da for fragment ions. Peptide identifications were filtered at 1% false discovery rate on peptide level using Percolator (Käll et al., 2007; Spivak et al., 2009).

Protein quantification from 1D-LC-MS^2 data

Peptide abundance was estimated by label-free quantification using the Progenesis QI for proteomics software (v2.0, Waters). Briefly, LC-MS^2 maps of all samples were aligned and peptides were quantified based on peak areas of precursor ions (full-scan FTMS). The MS^2 data associated to each precursor ion were exported from Progenesis as .MGF files (Mascot generic format) and used for peptide identification with the Proteome Discoverer software as outlined above. The peptide identifications were imported into Progenesis QI and matched to the corresponding feature across the different runs. Absolute protein abundance (fmol on-column) was estimated by the Hi3-based quantification method (Silva et al., 2006) using the known amount of spiked-in Hi3 ClpB protein standard. To determine the expression level (fmol/μg), the Mw of each protein was used to calculate the total on-column protein amount (μg) for each sample, followed by dividing individual protein fmol on-column amounts by the median total on-column protein amount across all samples. Following protein quantification, the results were further filtered to 1% false discovery rate on protein level by applying the standard target-decoy approach correcting for the use of separate protein target-decoy search results (Wang et al., 2009) as obtained using Proteome Discoverer.

Protein quantification from 2D-LC-MS^2 data

Peptide abundance in the 2D-LC-MS^2 data was also estimated by label-free quantification using Progenesis QI for Proteomics. Briefly, LC-MS^2 maps of individual fractions (10 per time point) were separately aligned and peptides were quantified based on peak areas of precursor ions (full-scan FTMS). The MS^2 data associated to each precursor ion were exported from Progenesis as .MGF files and used for peptide identification with the Proteome Discoverer software as outlined above. The peptide identifications

were re-imported into Progenesis QI and matched to the corresponding feature across the different fractions. The results of the 10 fractions were then combined into a single project file followed by label-free absolute quantification (fmol on-column) using the Hi3-based quantification method (Silva et al., 2006) and the known amount of spiked-in Hi3 ClpB protein standard. To determine the expression level (fmol/μg), the Mw of each protein was used to calculate the total on-column protein amount (μg) for each sample, followed by dividing individual protein fmol on-column amounts by the median total on-column protein amount across all samples. Following protein quantification, the results were further filtered to 1% false discovery rate on protein level by applying the standard target-decoy approach correcting for the use of separate protein target-decoy search results (Wang et al., 2009) as obtained using Proteome Discoverer. Finally, the two proteomics datasets were combined into a single file.

Statistical analysis and clustering of proteomics data

The inter-day Pearson correlation coefficient was calculated for averaged timelines of individual proteins (based on unique combination of accession and gene name) and independently for 1D-LC-MS^2 and 2D-LC-MS^2 data using SAS 9.4. Furthermore, statistical analysis by ANOVA of only the 1D-LC-MS^2 data was also carried out using SAS 9.4. Protein timelines with a p value less than 0.05 and an inter-day Pearson correlation greater than 0.66 were considered statistically significant. For the 2D-LC-MS^2 data the maximum fold-change was determined by dividing the maximum by the minimum protein abundance. Protein timelines with a maximum fold-change greater than 2 and an inter-day Pearson correlation greater than 0.66 were considered significant. For comparative visualization and clustering analysis, individual protein abundances were log2 transformed and converted to z-scores.

Statistically significant timelines of individual proteins obtained by 1D-LC-MS^2 analysis was analyzed by fuzzy c-means clustering using VSClust (Schwämmle and Jensen, 2018). The resulting centroid liver-protein timelines were subsequently compared using Pearson correlation to that of significant protein timelines obtained by the 2D-LC-MS^2 analysis. Significant protein timelines obtained by 2D-LC-MS^2 were allocated into distinct timeline clusters for which they have a Pearson correlation greater than 0.9. In a few instances we noted that an identical protein, detected by both 1D- and 2D-LC-MS^2 analysis, was grouped into two different clusters. In this case, we omitted the protein timeline obtained by 2D-LC-MS^2 analysis, since we only have two replicate values and not six as for the 1D-LC-MS^2 data.

Hierarchical clustering of centroid timeline clusters was carried out using ClustVis (Metsalu and Vilo, 2015) with Euclidean clustering distance and the Ward's clustering method. Statistical analysis of protein data shown in bar graphs is done using log2 transformation and by Student's t test in Excel (Microsoft).

Bioinformatics analysis of proteomics data

To shortlist lipid-related proteins we manually inspected the functionality of all protein members of the different clusters obtained by fuzzy c-means clustering. To do so, we downloaded and made use of information on functionality, subcellular location and gene ontologies from the UniProt database (Figure S5E).